Cellular/Molecular

Exocytotic Machineries of Vestibular Type I and Cochlear Ribbon Synapses Display Similar Intrinsic Otoferlin-Dependent Ca^{2+} Sensitivity But a Different Coupling to Ca^{2+} Channels

Philippe F.Y. Vincent,[1] Yohan Bouleau,[1] Saaid Safieddine,[2] Christine Petit,[2,3] and Didier Dulon[1]

[1]Université de Bordeaux, Institut des Neurosciences de Bordeaux, Equipe Neurophysiologie de la Synapse Auditive, Inserm, Unité Mixte de Recherche 1120, Centre Hospitalier Universitaire hôpital Pellegrin, 33076 Bordeaux, France, [2]Institut Pasteur et Université Pierre et Marie Curie, Unité de Génétique et Physiologie de l'Audition, Inserm Unité Mixte de Recherche 1120, 75015 Paris, France, and [3]Collège de France, 75005 Paris, France

The hair cell ribbon synapses of the mammalian auditory and vestibular systems differ greatly in their anatomical organization and firing properties. Notably, vestibular Type I hair cells (VHC-I) are surrounded by a single calyx-type afferent terminal that receives input from several ribbons, whereas cochlear inner hair cells (IHCs) are contacted by several individual afferent boutons, each facing a single ribbon. The specificity of the presynaptic molecular mechanisms regulating transmitter release at these different sensory ribbon synapses is not well understood. Here, we found that exocytosis during voltage activation of Ca^{2+} channels displayed higher Ca^{2+} sensitivity, 10 mV more negative half-maximum activation, and a smaller dynamic range in VHC-I than in IHCs. VHC-I had a larger number of Ca^{2+} channels per ribbon (158 vs 110 in IHCs), but their Ca^{2+} current density was twofold smaller because of a smaller open probability and unitary conductance. Using confocal and stimulated emission depletion immunofluorescence microscopy, we showed that VHC-I had fewer synaptic ribbons (7 vs 17 in IHCs) to which Cav1.3 channels are more tightly organized than in IHCs. Gradual intracellular Ca^{2+} uncaging experiments revealed that exocytosis had a similar intrinsic Ca^{2+} sensitivity in both VHC-I and IHCs (K_D of 3.3 $\pm$ 0.6 μM and 4.0 $\pm$ 0.7 μM, respectively). In otoferlin-deficient mice, exocytosis was largely reduced in VHC-I and IHCs. We conclude that VHC-I and IHCs use a similar micromolar-sensitive otoferlin Ca^{2+} sensor and that their sensory encoding specificity is essentially determined by a different functional organization of Ca^{2+} channels at their synaptic ribbons.

Key words: **auditory; exocytosis; hair cell; otoferlin; synapse; vestibular**

Introduction

Synaptic transmission at mammalian auditory and vestibular hair cell ribbon synapses shares several fundamental properties. In the auditory system, transmitter release occurs with high temporal precision and reliability to ensure phase-locking and spatial sound-localization (Kiang, 1965; Palmer and Russell, 1986). Similar high temporal precision and speed are required at vestibular hair cell synapses to trigger the ms-range vestibulo-ocular reflex (Huterer and Cullen, 2002). Furthermore, both types of hair cells must involve an indefatigable supply of synaptic vesicles to the ribbon to sustain high rates of transmitter release during endless ongoing stimulation (Fuchs, 2005; Eatock and Songer, 2011). Another common property is multivesicular release that produces large EPSCs to instantaneously drive afferents fibers to spike threshold (Glowatzki and Fuchs, 2002; Grant et al., 2010). Evidence for multivesicular release has also been reported in vestibular hair cells (Rennie and Streeter, 2006; Dulon et al., 2009).

Otoferlin, a C2 domain protein, is an essential Ca^{2+} sensor that controls transmitter release at the ribbon synapses of cochlear (Roux et al., 2006; Beurg et al., 2010; Pangrsic et al., 2010) and vestibular hair cells (Dulon et al., 2009). It has been suggested that otoferlin functions as a high-affinity Ca^{2+} sensor that linearizes exocytosis during voltage activation of Ca^{2+} channels in vestibular hair cells (Dulon et al., 2009). However, the intrinsic Ca^{2+} sensitivity of otoferlin in vestibular and cochlear hair cell synapses remains to be determined. In the present study, we used gradual uncaging Ca^{2+} experiments combined with whole-cell patch-clamp capacitance measurements to investigate the Ca^{2+} sensitivity of exocytosis in vestibular Type I hair cells (VHC-I) and cochlear inner hair cells (IHCs). Both types of hair cells differ greatly in the morphological organization of their afferent synapses. Notably, VHC-I are enveloped by a single large calyceal

Received March 10, 2014; revised June 22, 2014; accepted June 23, 2014.

Author contributions: P.F.Y.V. and D.D. designed research; P.F.Y.V., Y.B., and D.D. performed research; P.F.Y.V., Y.B., S.S., C.P., and D.D. analyzed data; P.F.Y.V. and D.D. wrote the paper.

We thank Ombeline de La Rochefoucauld for assistance in analyzing the Ca^{2+} chelator experiments under MATLAB software and Jean-Pierre Hardelin for critical reading of the manuscript.

The authors declare no competing financial interests.

Correspondence should be addressed to either Dr. Didier Dulon or Philippe Vincent, Université de Bordeaux, Institut des Neurosciences de Bordeaux, Equipe Neurophysiologie de la Synapse Auditive, Inserm, Unité Mixte de Recherche 1120, hôpital Pellegrin, 33076 Bordeaux, France, E-mail: didier.dulon@inserm.fr or philippe.vincent@inserm.fr.

DOI:10.1523/JNEUROSCI.0947-14.2014

 0270-6474/14/3410853-17$15.00/0

afferent ending that encodes the activity of several presynaptic ribbons (Eatock and Songer, 2011; Lysakowski et al., 2011; Songer and Eatock, 2013). On other hand, IHCs are contacted by 10–20 individual small afferent bouton endings (Liberman et al., 1990, 2011; Meyer et al., 2009), each bouton sensing the Ca^{2+}-dependent activity of a single ribbon (Goutman and Glowatzki, 2007). Cav1.3 channels are the main L-type Ca^{2+} channel subunits involved in synaptic exocytosis in both IHCs (Platzer et al., 2000; Brandt et al., 2003) and VHC-I (Dou et al., 2004). In IHCs, the membrane-associated Cav1.3 channels aggregate in small clusters in close spatial organization to the synaptic ribbons (Brandt et al., 2005), forming a spatially restricted Ca^{2+} microdomain at the active zone (Frank et al., 2009; Wong et al., 2014). However, neither the number of Ca^{2+} channels nor their spatial distribution at VHC-I calyx ribbon synapses has yet been explored. Here, we used various depolarizing protocols to investigate the functional organization of Ca^{2+} channels and the Ca^{2+} sensitivity of exocytosis in mouse VHC-I and IHCs. Furthermore, immunofluorescent confocal and stimulated emission depletion (STED) imaging were used to characterize the spatial organization of Cav1.3 channels in both types of hair cells.

Materials and Methods

Tissue preparation

Experiments were performed in accordance with the guidelines of the Animal Care Committee of the European Communities Council Directive (86/609/EEC) and the ethics committee of the University of Bordeaux. All mice (C57BL6 of either sex) were anesthetized by intraperitoneal injection of xylazine (6 mg/ml) and ketamine (80 mg/ml) mixture (Sigma-Aldrich) diluted in physiological saline. For calcium uncaging experiments, vestibular and cochlear organs were dissected from littermate controls (*Otof* $^{+/+}$, *Otof*$^{+/-}$) or from knock-out otoferlin (*Otof* $^{-/-}$) C57BL/6 mice as previously described (Dulon et al., 2009; Beurg et al., 2010).

Electrophysiological recordings from IHCs were obtained in whole-mount organ of Corti (OC) at postnatal day 12–14 (P12–P14), an age near the onset of hearing in mice (Ehret, 1983). In OC, all recordings were performed in the 20%–40% normalized distance from the apex, an area coding for frequencies ranging from 8 to 16 kHz (Meyer et al., 2009).

Electrophysiological experiments in VHC-I were performed in intact whole-mount utricles at postnatal day 5–7 (P5–P7), an age close to the onset of vestibular evoked potentials in mice (Jones and Jones, 2007; Lai et al., 2008). In the utricle, VHC-I were identified under contrast microscopy by their surrounding large calyceal afferent fiber as previously described (Dulon et al., 2009). All recordings were performed in the striola region of the utricles in which faster maturation of Type I hair cells occurs (Rüsch et al., 1998).

The OC or utricle was freshly dissected under binocular microscopy in an extracellular solution maintained at 4°C containing the following (in mM): 135 NaCl, 5.8 KCl, 1.3 $CaCl_2$, 0.9 $MgCl_2$, 0.7 NaH_2PO_4, 5.6 glucose, 2 Na pyruvate, 10 HEPES, pH 7.4, 305 mOsm. Tectorial membrane (OC) and otoconia (utricle) were carefully removed. The OC or the utricle was placed in a recording chamber and hair cells observed with a 60× water-immersion objective (CFI Fluor 60× W NIR, WD = 2.0 mm, NA = 1) attached to an upright Nikon FN1 microscope. The extracellular solution was complemented with 0.5 μM of apamin (Latoxan) and 0.2 μM of XE-991 (Tocris Bioscience) to block SK channels and KCNQ4 channels, respectively. The external Ca^{2+} concentration was increased from 1.3 to 5 mM to enhance the amplitude of Ca^{2+} currents. All experiments were performed at room temperature (22°C–24°C).

Whole-cell recording and capacitance measurement

All patch-clamp experiments were performed with an EPC10 amplifier controlled by pulse software Patchmaster (HEKA Elektronik). Patch pipettes were pulled with a micropipette Puller P-97 Flaming/Brown (Sutter Instrument) and fire polished with a Micro forge MF-830 (Narishige) to obtain a resistance range from 3 to 5 MΩ. Patch pipettes were filled with intracellular solution containing the following (in mM): 145 CsCl, 1 $MgCl_2$, 5 HEPES, 1 EGTA, 20 TEA, pH 7.2, 300 mOsm. Our recording solution was ATP and GTP free to prevent the activation of P2Y-P2X receptors when approaching the patch -pipette with positive pressure near the cells, but also to reduce intracellular Ca^{2+} buffering by nucleotides. The absence of ATP and GTP in the intracellular patch pipette did not change Ca^{2+} currents and exocytosis when limiting: (1) the whole-cell recording time to 5–7 min after break-in; and (2) the voltage stimuli to a short period <100 ms. Exocytotic responses shown in the present studies are comparable with our previous studies where 5 mM ATP and 0.5 mM GTP were present in the recording solutions (Dulon et al., 2009; Beurg et al., 2010). Because the sensory organs are continuously bathing in an extracellular medium with Na-pyruvate and glucose, we think that hair cells produce and contain enough intrinsic intracellular ATP to sustain brief RRP exocytotic responses.

Ramp stimulation. Cells were maintained at −80 mV and depolarized from −90 mV to 30 mV in 120 ms giving a slope of voltage change of 1 mV/ms.

Counting of Ca^{2+} channels. The number of Ca^{2+} channels in VHC-I and IHCs was determined by using the nonstationary fluctuation analysis of tail current previously described by Roberts et al. (1990). Tail currents were recorded at −62 mV after a 15 ms depolarization step from −100 mV (holding potential) to 30 mV (maximum of open channels). This protocol was repeated 500 times at intervals of 80 ms. Measurement of variance was performed after rescale of each of the 500 peaks of tail current to the maximum peak observed. Variance was calculated with the following formula (Roberts et al., 1990; Brandt et al., 2005):

$$\sigma^2(t) = 1/(2K - 1)\sum_{i-1}^{K-1}[X_i(t) - X_{i+1}(t)]^2$$

where K is the number of stimuli used (500) and $x_i(t)$ is the leak subtracted response to the *ith* stimulus. After plotting the variance versus the mean of tail currents (I_{mean}), data points were fitted using the following formula:

$$var = iI_{mean} - (I_{mean}{}^2/N)$$

where i is the unitary current and N the number of Ca^{2+} channels. Tail-current recordings were performed in extracellular solution with 10 mM Ca^{2+} and 1 mM Ba^{2+} and 5 μM BayK8644, a dihydropiridine agonist increasing the open probability of Ca^{2+} channels (Brown et al., 1984; Brandt et al., 2005).

Real-time capacitance measurement. Membrane capacitance measurements (C_m) were performed using the Lock-in amplifier Patchmaster software (HEKA) by applying a 1 kHz command sine wave (amplitude 20 mV) at holding potential (−80 mV) before and after the pulse experiment. Because capacitance measurement requires high and constant membrane resistance (R_m) (Johnson et al., 2005), the amplitude of the sine wave was small enough to avoid activation of significant membrane current. Exocytosis (Δ_{Cm}) was calculated by subtracting the average capacitance measurement 60–100 ms after the depolarizing pulse (end of tail current) and the average capacitance measurement 50 ms before the pulse as baseline.

Voltage stimulation. Two protocols were used. First, a protocol probing the kinetics of exocytosis where the cells were depolarized from −80 mV to −10 mV for increasing time duration from 10 to 120 ms in 10 ms increments. Second, a protocol probing the voltage dependence of exocytosis where the cells were depolarized from −90 mV to 5 mV in 5 mV increments for a constant 25 ms duration. Only cells with stable R_m, leak current <50 pA at holding potential (−80 mV) and stable series resistance <20 MΩ were considered in the study. All Ca^{2+} currents were leak subtracted by using a linear function calculated from the leak current at holding potential (−80 mV) and the approximated reversal potential of the leak current (Brandt et al., 2005).

Calcium charge (Q_{Ca}) measurement. The Ca^{2+} charge was calculated with Patchmaster software by integrating the area from the start of the Ca^{2+} current to the end of the Ca^{2+} tail current.

Ca^{2+} chelator experiments

We evaluated the coupling distance between Ca^{2+} channels and Ca^{2+} sensors by testing the concentration dependence of two Ca^{2+} chelators (EGTA and BAPTA) on the Ca^{2+} efficiency of exocytosis (Δ_{Cm}/Q_{Ca}). Data points were fitted using the linearized reaction diffusion equation assuming that the saturation of exogenous buffer was negligible (Neher, 1998; Bucurenciu et al., 2008) as follows:

$$\Delta_{Cm}/Q_{Ca} = \exp(-r/\lambda_b)/\exp(-r/\lambda_0)$$

$$\lambda_0 = \sqrt{D_{Ca}/(K^o_{on}[B]^o)}$$

$$\lambda_b = \sqrt{D_{Ca}/(K^o_{on}[B]^o + K^b_{on} B^b_T K^b_D/([Ca^{2+}]^n_r + K^b_D))}$$

where r is the distance between the Ca^{2+} channels and the sensor, D_{Ca} is the diffusion coefficient of free Ca^{2+}, $K^o_{on}[B]^o$ is the buffer product of endogenous buffer, K^b_{on} is the rate constant of Ca^{2+} binding to exogenous buffer, B^b_T is the total concentration of exogenous Ca^{2+} buffer, K^b_D is dissociation constant of exogenous buffer, $[Ca^{2+}]^n_r$ is the resting Ca^{2+} concentration and n the Hill cooperativity coefficient of otoferlin. We assumed that physicochemical properties follow those previously described (Bucurenciu et al., 2008; Vyleta and Jonas, 2014): $D_{Ca} = 220\ \mu m^2 \cdot s^{-1}$, $K^b_{on} = 4 \times 10^8\ M^{-1} \cdot s^{-1}$ for BAPTA and $1 \times 10^7\ M^{-1} \cdot s^{-1}$ for EGTA, $K^b_D = 0.22\ \mu M$ for BAPTA and 0.07 μM for EGTA. $[Ca^{2+}]^n_r$ has been determined by using AM loaded dye in frog saccular hair cells (Hall et al., 1997) and is assumed to be 1×10^{-7} M in IHCs and VHC-I. The coefficient of cooperativity (n) was set at 3 (see our Fig. 9). $K^o_{on}[B]^o$ was determined as $[B]_{endo} \times E_{on} = 9 \times 10^7\ M^{-1} \cdot s^{-1} \times 0.001\ M = 9000\ s^{-1}$ in VHC and $9 \times 10^7\ M^{-1} \cdot s^{-1} \times 0.003\ M = 2700\ s^{-1}$ in IHCs. $[B]_{endo}$ is the concentration of endogenous buffer (1 mM in VHC; Hall et al., 1997; 0.3 mM in IHCs; Hackney et al., 2005). E_{on} is the on rate constant of Ca^{2+} binding to endogenous buffer ($9 \times 10^7\ M^{-1} \cdot s^{-1}$; Hall et al., 1997). We assumed that E_{on} is equal in both VHC-I and IHCs.

Caged Ca^{2+} photolysis and Ca^{2+} concentration measurement

To trigger a progressive step-increase in the intracellular Ca^{2+} concentration from the caged Ca^{2+} chelator DM-nitrophen (Interchim), we used brief flashes from a UV LED light source (Mic-LED 365, 128 mW, Prizmatix). The UV LED was directly connected to the epi-illumination port at the rear of the upright Nikon FN1 microscope and illumination focalized through the 60× objective (CFI Fluor 60× W NIR, WD = 2.0 mm, NA = 1). Changes in $[Ca^{2+}]_i$ were continuously measured with a C2 confocal system and NIS-elements imaging software (Nikon) coupled to the FN1 microscope. The low-affinity Ca^{2+} dye Oregon Green Bapta-5N (OGB-5N, $K_D = 20\ \mu M$, Invitrogen) was used as intracellular calcium probe. The dye was excited with a 488 nm solid-state laser (85-BCD-010-706, Melles Griot) and emission recorded at 500–530 nm. We used OGB-5N because there is no photolysis of DM-nitrophen with visible-light excitation at 488 nm. This allowed continuous monitoring of Ca^{2+} signals during the multi UV flash protocol.

For simultaneous Ca^{2+} uncaging and OGB-5N-$[Ca^{2+}]_i$ experiments, in which membrane capacitance was continuously recorded, patch pipettes were filled with the following solution (in mM): 145 CsCl, 5 HEPES, 20 TEA, 10 DM-nitrophen, 10 $CaCl_2$, 0.05 OGB-5N. After rupture of the patch, we waited systematically for 2 min at holding potential of −70 mV to load and equilibrate the cells. Thirteen TTL-triggered 10 ms UV flashes 200 ms apart were then applied to the cells. These brief successive flashes allowed a progressive step-increase in $[Ca^{2+}]_i$ from up to 20 μM. The 200 ms interval between each TTL-UV flash was meant to allow nearly complete vesicular replenishment to the ribbon, as estimated by Levic et al. (2011). OGB-5N-emission fluorescence was analyzed by the ratio F/F_{max} ratio, where F_{max} is the maximum fluorescence found with *in vivo* calibration in each cell type. The instantaneous rate of release was measured by fitting the first 20 ms of the response after each flash, thereby giving the rate of the ready release component (RRP) at each concentration of Ca^{2+}.

In some experiments, endocytosis was measured in hair cells loaded with the following (in mM): 145 CsCl, 5 HEPES, 20 TEA, 10 DM-nitrophen, 10 $CaCl_2$, and flashed with a high energy UV illumination system connected to the rear of the FN1 microscope (Nikon Intensilight C-HGFI, HG lamp 130 W, excitation 330–380 nm). In these conditions, using the low-affinity Ca^{2+} dye Fluo-5N ($K_D = 90\ \mu M$; Invitrogen), $[Ca^{2+}]_i$ was measured to jump directly to 80 μM.

In vivo calibration of OGB-5N. We performed an *in vivo* calibration of the Ca^{2+}-dependent fluorescent signal of OGB-5N. Hair cells were voltage-clamped at −70 mV in whole-cell configuration with different solutions containing various free calcium concentrations ($[Ca^{2+}]_{free}$) from 1 to 100 μM. The patch pipettes were filled with a Cs-based solution (in mM: 145 CsCl, 5 HEPES, 20 TEA, 0.05 OGB-5N) and different concentration of Ca^{2+} and EGTA. The freeware Ca-EGTA Maxchelator was used to determine $[Ca^{2+}]_{free}$. After 2 min of cell loading and equilibrium, the fluorescence signal was measured at each $[Ca^{2+}]_{free}$ in different VHC-I and IHCs (Fig. 7*A*,*B*). Fluorescence emission values were plotted as F/F_{max} against $[Ca^{2+}]_{free}$. Data points were best fitted by using a sigmoidal function with a K_D of 13.81 ± 1.81 μM and 23.30 ± 0.71 μM in VHC-I and IHCs, respectively. These K_D values are very close to the value reported *in vitro* ($K_D = 20\ \mu M$, Molecular Probes, Invitrogen). Intracellular $[Ca^{2+}]$ obtained after each UV flash was calculated by using the following formula:

$$[Ca^{2+}]_i = K_D (F - F_{min})/(F_{max} - F)$$

where K_D is the respective *in vivo* constant of dissociation measured in VHC-I and IHCs (Fig. 7*A*,*B*), F is the fluorescence at time t, F_{min} is the minimum fluorescence, and F_{max} is the maximal fluorescence.

Immunohistofluorescence

Preparation of tissues. The ramps of the cochlear and vestibular apparatus of P12–P14 mice were rapidly perfused with 100% methanol at −20°C for 30 min and washed with cold PBS. The inner ear was then incubated for 2 h in PBS solution containing 10% EDTA. The OC and utricle were then dissected and the tectorial membrane and otoconia removed. Tissues were first incubated with PBS containing 30% normal horse serum for 1 h at room temperature. Then, they were incubated with primary antibodies diluted with PBS (1:200) containing 5% horse serum and 0.1% Triton X-100. Synaptic ribbons, Cav1.3 channels, and otoferlin were simultaneously labeled with anti-CtBP2 (goat polyclonal, Santa Cruz Biotechnology; catalog #SC-5966), anti-Cav1.3 (rabbit polyclonal, Alomone Labs; catalog #ACC-005) and anti-otoferlin (mouse monoclonal, AbCam, Paris, France; catalog #ab53233) antibodies, respectively. Actin-F was also used to visualize hair cells (1:100, Phalloidin Fluoprobe 405, Interchim; catalog #FP-CA9870). In some experiments, anti-otoferlin antibodies were replaced by anti-NF200 antibodies to identify the afferent calyceal processes around VHC-I. The OC and utricle were then washed with PBS and incubated in two steps with secondary antibodies at 1:500: first donkey anti-goat Fluoprobe 547H (Interchim; catalog #FP-SB2110) and donkey anti-mouse Fluoprobe 647 (Interchim; catalog #FP-SC4110), second after PBS rinse with goat anti-rabbit AlexaFluor-488 (Invitrogen; catalog #A-11008). Surface preparations of OC (apical turns) and utricles were then mounted on Superfrost-Plus glass slides (Kindler) in a Prolong-Antifade medium (Invitrogen) and kept in the dark at −20°C until observation. All immunoreactions in utricles and OC were performed simultaneously on the same days in rigorously identical conditions.

Image acquisition. Fluorescence images of utricles and OC were also acquired in parallel with identical confocal imaging parameters during the same imaging sessions. The experiments were repeated 5 times in different mouse dissections and immunoreactions.

Samples were analyzed using a confocal laser scanning microscope Leica SP8 with a 63× oil-immersion objective (NA = 1.4) and white light laser (470–670 nm) (Bordeaux Imaging Center). Wavelengths were selected by an acousto-optical tunable filter (AOTF) associated with a photonic crystal fiber. This combination allowed precise selection of multiple wavelengths simultaneously. Phalloidin was imaged by using a diode laser at 405 nm also mounted on the microscope.

Stack images were acquired with the following parameters: laser power 40%, scan rate 700 Hz, scans averaged per *X*-*Y* section 4 times, step size 250 nm, pixel size 80 nm giving an *X*-*Y* image size of 41 × 41 μm (512 × 512 pixels). Images were then processed for 3D blind deconvolution with AutoQuant X2 (MediaCybernetics). After deconvolution, images were

processed under ImageJ software (W.S. Rasband, National Institutes of Health) and 3D-reconstructed for volume and surface area measurements with Imaris software (Bitplane AG).

Image calibration. We used fluorescent microbeads as references to calibrate confocal analysis of the Cav1.3 and CtBP2 signals. Fluoresbrite yellow-green carboxy-microspheres (mean diameter of 0.490 ± 0.004 μm; Polysciences) with excitation and emission spectra close to Alexa-488 were used to calibrate Cav1.3 labeling. Fluoresbrite YO carboxy-microspheres (0.487 ± 0.011 μm; Polysciences), with excitation and emission spectra close to Fluoprobe 547H, were used to calibrate CtBP2 labeling. A diluted mixture of YG and YO beads was mounted between slide and coverslip in a mounting medium similar to that used for tissue samples. Confocal imaging of beads was done the same day and with the same confocal parameters as with tissue samples. Bead stack images were 3D-deconvoluted and 3D-reconstructed under the same conditions as for tissue samples. 3D-reconstructed images appeared as ellipsoid objects rather than as the expected spherical beads, suggesting image distortion. We therefore estimated the correcting factors for oblate (*X-Y*) and prolate (*Z*) radius. We found that the *X-Y* measured diameters (80 nm resolution) differed from real values by a factor of 1.21 and 1.00 in YG ($n = 43$) and YO beads ($n = 180$), respectively. In *Z*-directions and at a lower resolution of 250 nm, YG and YO diameters differed by a factor 2.11 and 3.01, respectively. All Cav1.3 and CtBP2 images were then corrected using these respective factors. Ribbon volumes were assessed by using the following formula: $V = 4/3\ \pi\, r^2_{oblate}\, r_{prolate}$ and Cav1.3 surface areas with $S = \pi\, r^2_{oblate}$.

Colocalization of Cav1.3 channels and ribbons. Colocalization (center mass distance) was analyzed by the distance objects based methods with the JACoP plugin (Bolte and Cordelières, 2006; Di Biase et al., 2008) in ImageJ (W.S. Rasband, National Institutes of Health).

STED microscopy. For high-resolution imaging of Cav1.3 channels clusters at VHC-I and IHC ribbons, we used a Leica DMI6000 TCS SP5 STED microscope with 100X objective (NA 1.4) (Bordeaux Imaging Center). Mouse P21 sensory organs were fixed and incubated with primary anti Cav1.3 (1/100) and CtBP2 (1/100) antibodies in conditions similar to those described above for confocal microscopy. Secondary antibodies goat anti-rabbit Atto 647N (Sigma-Aldrich, catalog #40839; 1/200) and chicken anti-goat Alexa-594 (Invitrogen, catalog #A-21468; 1/200) were used to label anti-Cav1.3 and-CtBP2 primary antibodies, respectively. Two-color STED microscopy used two lasers with excitation wavelengths of 532 and 635 nm. The pulsed STED depletion laser (pulsed laser IR, Spectra Physics Mai Tai) was set at 750 nm. Stack images were acquired with the following parameters: scan rate 100 Hz, scans averaged per *X-Y* section 8 times, pixel size 20 nm giving an *X-Y* image size of 21 × 21 μm (1024 × 1024 pixels). Image analysis was performed with ImageJ software.

Statistical analysis

Electrophysiological results were analyzed with Patchmaster (HEKA Elektronik), OriginPRO 9.1 (OriginLab), and IgorPro 6.3 (Wavemetrics). Results are expressed as mean ± SEM. Statistical analyses were performed by using Student's *t* test. The limit of significance was set at 0.05 ($p < 0.05$).

Results

Density and voltage dependence of Ca^{2+} currents

The voltage-ramp protocol revealed much larger global Ca^{2+} currents (I_{Ca}) in IHCs than in VHC-I (Fig. 1*A*). Maximum I_{Ca} had a mean value of −53.33 ± 6.69 pA ($n = 7$) and 190.13 ± 18.70 pA ($n = 10$) in VHC-I and IHCs, respectively ($p < 0.001$). Because run-up of the Ca^{2+} current can be observed after break-in during whole-cell recording in hair cells (Schnee and Ricci, 2003), I_{Ca} amplitudes were systematically measured after stabilization of the run-up period (i.e., 2–3 min after rupturing the patch membrane in our experimental conditions). The amplitudes of the Ca^{2+} currents are in good agreement with previous studies in mouse VHC-I (Bao et al., 2003; Dulon et al., 2009) and IHCs (Brandt et al., 2005; Johnson et al., 2005; Beurg et al., 2010).

Notably, we found that the cell membrane surface area of VHC-I was twofold smaller than IHCs as indicated by their respective membrane capacitance of 5.28 ± 0.15 pF and 9.32 ± 0.34 pF, respectively (Fig. 1*F′*). Therefore, membranous I_{Ca} density (pA/pF) was calculated to be twofold larger in IHCs than in VHC-I (VHC-I = −10.10 ± 1.26 pA/pF; IHCs = −20.39 ± 2.03 pA/pF; $p < 0.001$, Fig. 1*A* inset). Fitting the IV-ramp curve with a sigmoidal Boltzmann function ($I_{(V)} = I_{max}/1 + \exp[(V_{1/2} - V)/k]$), between −70 mV and −10 mV, indicated a more negative half-maximal voltage activation potential ($V_{1/2}$) in VHC-I (−33.11 ± 1.65 mV) than in IHCs (−27.07 ± 0.73 mV, $p < 0.05$). The slope of the Boltzmann function showed a similar relationship between channel activation and voltage with k = 6.18 ± 0.22 pA/mV and k = 5.56 ± 0.28 pA/mV in VHC-I and IHCs, respectively ($p = 0.22$).

The total number of Ca^{2+} channels in VHC-I and IHCs was then assessed by nonstationary fluctuation analysis of tail currents as previously described (Roberts et al., 1990; Brandt et al., 2005). Cells were depolarized to 30 mV and tail currents recorded at −62 mV (Fig. 2). Variance analysis of tail currents gave a total number of Ca^{2+} channels *N* of 1175 ± 96 ($n = 17$) and 1848 ± 80 ($n = 11$) associated with a single-channel current *i* of 0.32 ± 0.02 pA and 0.51 ± 0.01 pA in VHC-I and IHCs, respectively ($p < 0.05$ for *N* and *i*). Using the relationship $I = i.N.p$, where *I* is the macroscopic tail current, we found an open probability *p* of 0.82 ± 0.02 and 0.81 ± 0.03 (p_{max} in presence of BayK8644) in VHC-I and IHCs, respectively ($p = 0.71$). Our estimates of channel number and conductance in IHCs are similar to the value previously reported by Brandt et al. (2005). Our present study, constituting the first estimate of the total number of Ca^{2+} channels in VHC-I, indicated that there was ~36.4% fewer Ca^{2+} channels in VHC-I than in IHCs.

Using quantitative immunofluorescent confocal imaging of ribbons stained with a CtBP2 antibody, we then determined the number of synaptic ribbons in each cell type (Fig. 1*E′*; see Fig. 4). VHC-I displayed nearly twofold fewer ribbons than in IHCs: 7.4 ± 0.8 ($n = 49$ VHC-I) and 16.5 ± 2.5 ($n = 16$ IHCs), respectively ($p < 0.05$; Fig. 1*E′*). These ribbon numbers per IHCs and VHC-I are consistent with the previous findings of Meyer et al. (2009) and Dulon et al. (2009), respectively. Assuming that all Ca^{2+} channels are clustered to the ribbons, we calculated a total number of 158 ± 12 and 110 ± 5 Ca^{2+} channels per ribbon in VHC-I and IHCs, respectively ($p < 0.05$). Considering the macroscopic current at −10 mV in 5 mM external Ca^{2+} (Fig. 1*A*), the single-channel current, and total number of channels (Fig. 2), we calculated a maximal open probability of 14.0 ± 1.0% and 21.0 ± 0.9% in VHC-I and IHCs, respectively ($p < 0.05$). A low open probability of Ca^{2+} channels similar to VHC-I was previously reported in immature IHCs (Zampini et al., 2010).

Considering their respective open probability at −10 mV in 5 mM external Ca^{2+}, we therefore estimated a number of open channels per ribbon synapse that was similar in VHC-I and IHCs (22.1 ± 3.5 and 22.3 ± 1.2, respectively, $p = 0.46$). Our results in IHCs are in agreement with those of Brandt et al. (2005) who estimated a total of 80 Ca^{2+} channels per IHCs synapse in which 20 channels are open simultaneously at −20 mV. Similar numbers were found in frog saccular hair cells (Roberts et al., 1990), turtle cochlear hair cells (Wu et al., 1996), hair cells of the amphibian papillae (Graydon et al., 2011), and salamander cones (Bartoletti et al., 2011), suggesting that there is a rather constant number of Ca^{2+} channels per ribbon release site.

By fitting the tail current decay with a single exponential, we found a faster deactivation of Ca^{2+} currents in VHC-I than in IHCs (0.53 ± 0.1 ms and 1.40 ± 0.7 ms, respectively, $p < 0.001$).

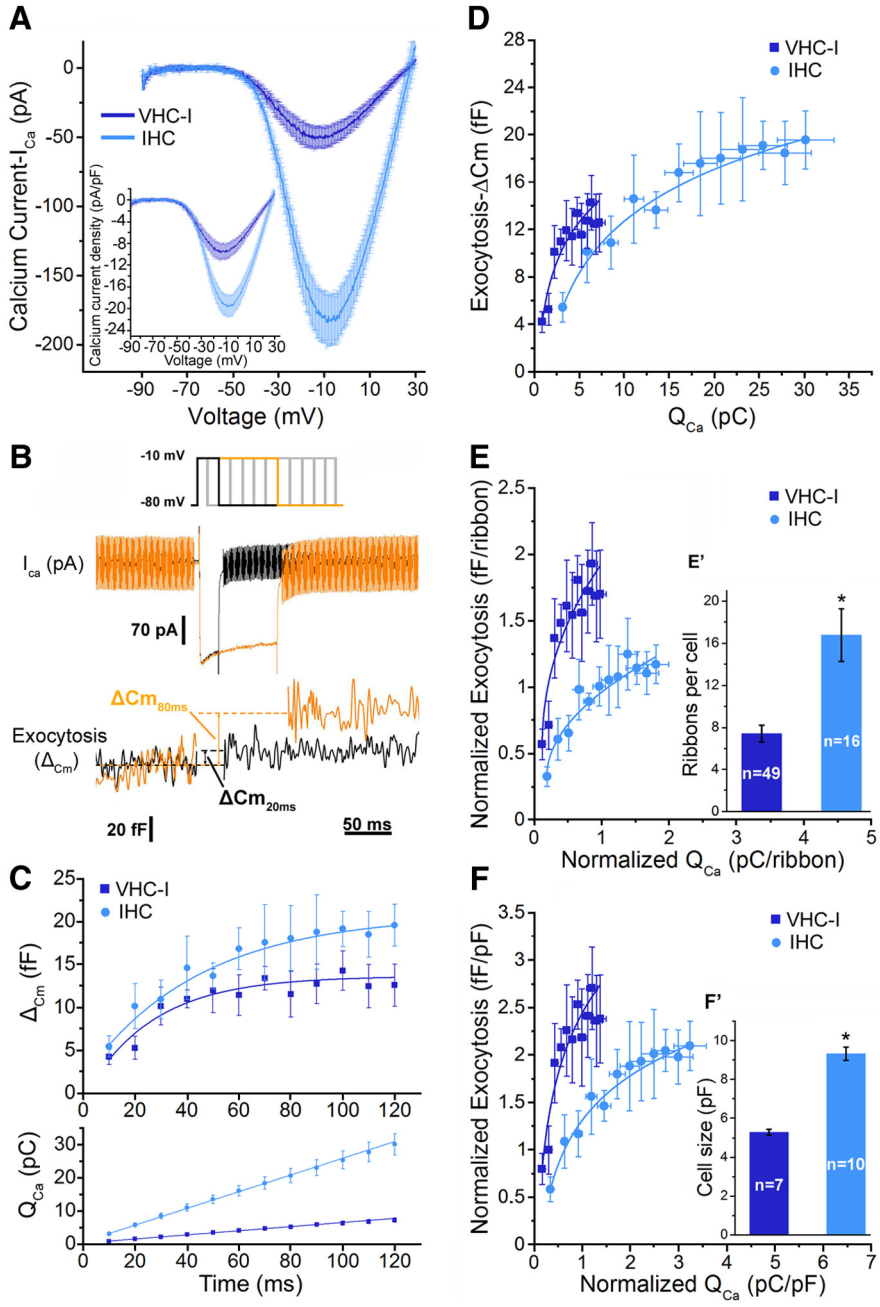

Figure 1. Kinetics of RRP release in Type I vestibular hair cells (VHC-I, dark blue) and inner hair cells (IHCs, light blue). ***A***, IV-ramp activation curve of Ca^{2+} currents in VHC-I ($n = 7$) and IHCs ($n = 10$) from −90 mV to 30 mV (1 mV/ms). Inset, Ca^{2+} current density relative to cell size (pA/pF). ***B***, Examples of I_{Ca} and capacitance measurements (Δ_{Cm}) in IHCs for 20 ms (black) and 80 ms (orange) depolarization duration. Cells were depolarized from holding potential −80 mV to −10 mV with various time durations (from 10 to 120 ms). ***C***, Δ_{Cm} values were plotted against depolarization duration (top). Data were best fitted with a monoexponential function where $\tau = 35.7 \pm 5.7$ ms ($n = 7$) and $\tau = 35.4 \pm 6.3$ ms ($n = 9$) in VHC-I and IHCs, respectively. Bottom, Ca^{2+} current charge integrals (Q_{Ca}) plotted against time (linear fit). ***D***, Δ_{Cm} values plotted against Q_{Ca} (data from ***C***) were fitted with a simple power function with index of 0.51 and 0.46 in VHC-I and IHCs, respectively. ***E***, Δ_{Cm} values plotted against Q_{Ca} normalized to the number of ribbon (***E'***). ***F***, Δ_{Cm} values plotted against Q_{Ca} to cell size (***F'***). Error bars indicate SEM. *$p < 0.05$.

These "nonphysiological" slow deactivation time constants are due to the dihydropiridine agonist BayK8644. This molecule has indeed been described to increase the deactivation τ decay from 0.1 ms to 1.2 ms in chick hair cells by Zidanic and Fuchs (1995).

Taken together with a more negative voltage dependence and a lower single-channel current, our results suggest the involvement of different composition of Ca^{2+} channels in VHC-I, possibly due to the expression of different regulatory subunits and/or α-subunit isoforms. However, the increased open probability from 0.14 or 0.21 to ~0.82 in the presence of BayK8644 suggests that most of the Ca^{2+} channels in both VHC-I and IHCs belong to the L-type Ca^{2+} channel family.

Kinetics of RRP exocytosis: Ca^{2+} efficiency and dynamic range

To characterize the dynamics of the readily releasable pool of vesicles (RRP), IHCs and VHC-I were depolarized by a single voltage-step from −80 mV to −10 mV of increasing duration from 10 to 120 ms (Fig. 1*B*,*C*). This single voltage-step to −10 mV was chosen to instantaneously reach maximal voltage activation of Ca^{2+} channels (Fig. 1*A*). Increasing the duration of depolarization from 10 to 120 ms at constant voltage made it possible to compare the Ca^{2+} sensitivity of RRP exocytosis (Δ_{Cm}) in both types of hair cells in regards to the size of the Ca^{2+} microdomain, independently of the respective contributions of the number of open channels and Ca^{2+} flux per channel. Using the data of Wu et al. (1996; their Fig. 3), this protocol would theoretically increase, with 1 mM EGTA as diffusible buffer, the size of the Ca^{2+} domain from a maximal radius of 450 nm at 10 ms ($[Ca^{2+}]_i$-450 nm ~80 μM) to ~1400 nm at 120 ms ($[Ca^{2+}]_i$-1400 nm ~10 μM). Inside each microdomain, $[Ca^{2+}]_i$ is considered to drop exponentially with distance from Ca^{2+} channels (Naraghi and Neher, 1997). Fixed Ca^{2+} buffers as well as diffusion barriers, such as the docked vesicles and the ribbon itself, would also influence the steady-state $[Ca^{2+}]$ profile near the Ca^{2+} channels (Graydon et al., 2011).

The plot of Δ_{Cm} as a function of time indicated an exponential rise with similar time constants in VHC-I and IHCs (Fig. 1*C*; $\tau = 35.7 \pm 5.7$ ms; $\tau = 35.4 \pm 6.3$ ms, respectively, $p = 0.97$). Δ_{Cm} responses reached a plateau at 12.58 ± 2.44 fF and 19.87 ± 2.45 fF in VHC-I and IHCs ($p = 0.069$), respectively. By normalizing the RRP to their respective number of ribbon, we estimated a similar value of 1.70 ± 0.25 and 1.19 ± 0.14 fF/ribbon in VHC-I and IHCs, respectively ($p = 0.15$). Considering a value of 34 aF per vesicle (Lenzi et al., 1999), the total number of vesicles per ribbon involved in the RRP exocytosis was calculated to be 50.0 ± 7.4 and 34.5 ± 4.1 in VHC-I and IHCs, respectively ($p = 0.15$). These values are similar to the 50–60 release ready vesicles per synaptic ribbon previously estimated in IHCs (Brandt et al., 2005). Considering a total number of 158 and 110 Ca^{2+} channels per ribbon synapses in VHC-I and IHCs, respectively, we calculated the involvement of ~3 Ca^{2+} channels per vesicle in both cell types. A similar number

of 2–3 Ca^{2+} channels openings per vesicle fusion event at each ribbon has been previously estimated in salamander cones (Bartoletti et al., 2011).

Remarkably, the Ca^{2+} current charge entry (Q_{Ca}), calculated at each step-duration, linearly increased with time in both type of hair cells (Fig. 1*C*). This indicated the absence of Ca^{2+} current inactivation in both cell types. However, the Q_{Ca} increase showed a fourfold smaller slope in VHC-I than in to IHCs (0.057 ± 0.005 pC/ms and 0.243 ± 0.026 pC/ms, respectively; $p < 0.001$). The Ca^{2+} efficiency of exocytosis was then obtained by plotting Δ_{Cm} responses as a function of Q_{Ca}. Data were fitted with a power function: $\Delta_{Cm} = y_0 + A\,[x - x_c]^a$ with A = Ca^{2+} efficiency slope; $x_c = Q_{Ca}$ threshold, a = power cooperative index, and y_0 = initial value. A similar low-power index function with $a = 0.51 \pm 0.04$ and 0.46 ± 0.06 was found in VHC-I and IHCs, respectively ($p = 0.45$). This convex (supralinear) relationship indicated an apparent noncooperative relationship between exocytosis and cumulative Ca^{2+} entry in both types of hair cells. This convex behavior may be due to the coexistence of two regimes of exoctytosis: a regimen based on independent Ca^{2+} nanodomains and a regimen based on an increasing Ca^{2+} "shell domain" (microdomain) when the activity of the nanodomains overlaps and linearly sums up during long depolarization. A similar sublinear relationship with a power index of ~0.78 was reported in auditory hair cells of the bullfrog amphibian papilla when varying external Ca^{2+} concentrations at constant voltage (Cho et al., 2011). A quasi-linear exocytosis was observed in IHCs when varying the number of open Ca^{2+} channels, suggesting a nanodomain-like control of exocytosis in these conditions (Johnson et al., 2005; Wong et al., 2014).

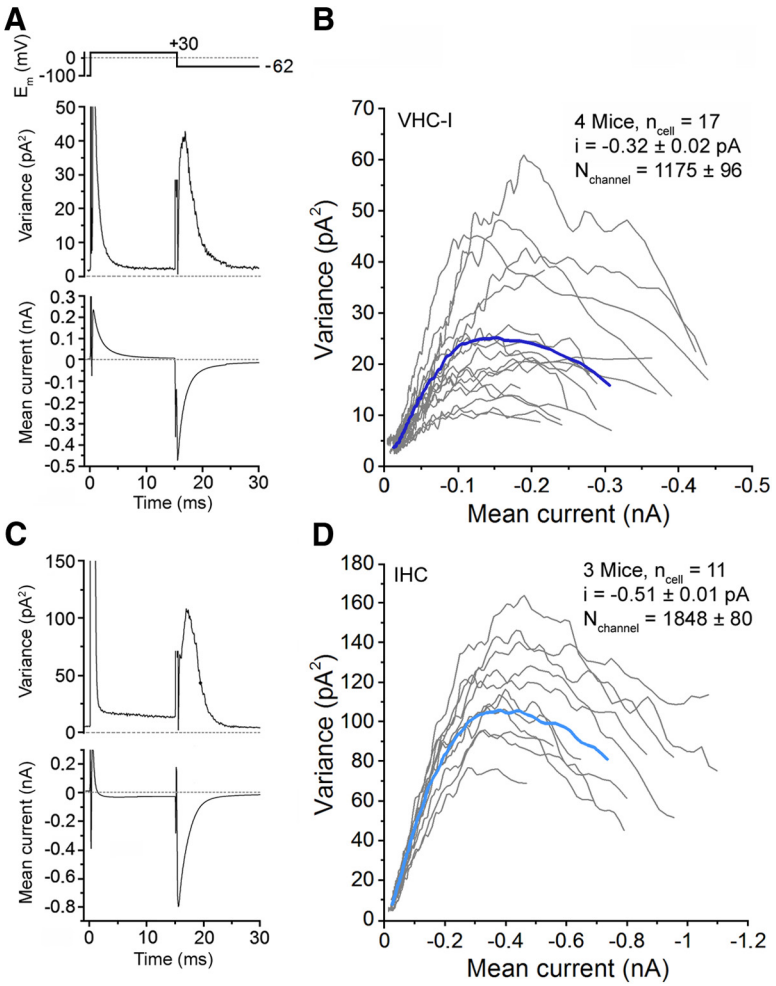

Figure 2. Counting Ca^{2+} channels in VHC-I and IHCs. Variance analysis of Ca^{2+} tail currents were performed from an ensemble of 500 sweeps (interval, 80 ms) after leak subtraction in one example of VHC-I (***A***) and IHCs (***C***). The plot of the variance against the current represents a characteristic parabolic relationship in VHC-I (***B***) and IHCs (***D***). Gray lines indicate the response of individual cells. Dark blue (VHC-I, ***B***) and light blue (IHCs, ***D***) lines indicate the average of each cell type. n_{cell}, Number of cells; *i*, unitary current; $N_{channel}$, number of Ca^{2+} channels. Recordings were performed in presence of 10 mM Ca^{2+}, 1 mM Ba^{2+}, and 5 μM BayK8644.

We found here that the Ca^{2+} efficiency slope (A) was larger in VHC-I than IHCs with A = 5.09 ± 1.19 fF/pC and 2.06 ± 0.69 fF/pC ($p < 0.05$), respectively (Fig. 1*D*). Remarkably, the IHCs Ca^{2+} efficiency slope is comparable with the maximum Ca^{2+} efficiency of exocytosis (3.0 fF/pC) found in frog auditory hair cells (Graydon et al., 2011). However, the higher Ca^{2+} efficiency slope that we observed here for VHC-I indicated that the mobilization of the RRP is more efficient in VHC-I than in IHCs. Notably, exocytosis in VHC-I covered a much smaller Ca^{2+} dynamic range than in IHCs (6.36 ± 0.59 pC and 27.02 ± 2.87 pC, respectively; $p < 0.001$). When normalizing Δ_{Cm} and Q_{Ca} responses to ribbon numbers, Ca^{2+} efficiency of exocytosis per ribbon synapse was estimated to be 1.73 ± 0.43 fF/pC and 0.68 ± 0.12 fF/pC in VHC-I and IHCs, respectively ($p < 0.05$; Fig. 1*E*). Furthermore, when normalizing Δ_{Cm} and Q_{Ca} responses to the cell surface membrane area (C_m in pF), Ca^{2+} efficiency of exocytosis was found to be 2.08 ± 0.39 fF/pC and 1.03 ± 0.64 fF/pC in VHC-I and IHCs, respectively ($p < 0.05$; Fig. 1*F*). The Q_{Ca} dynamic range of exocytosis per ribbon was nearly twofold smaller in VHC-I (0.85 ± 0.08 pC/ribbon) than in IHCs (1.62 ± 0.17 pC/ribbon; $p < 0.05$). Overall, these results showed that the temporal mobilization of RRP vesicles at the ribbon has similar kinetics in VHC-I and IHCs. However, RRP exocytosis in IHCs required a much larger Ca^{2+} influx. This could be explained either by a different Ca^{2+} sensitivity of the exocytotic sensor, by a different Ca^{2+} single-channel conductance or by a different spatial organization of Ca^{2+} channels with regards to the Ca^{2+} sensor. Because VHC-I showed a lower elementary Ca^{2+} current with lower open probability, the intrinsic property of the Ca^{2+} channel current could not account for the higher Ca^{2+} efficiency of RRP exocytosis in VHC-I than in IHCs. Therefore, considering a similar number of open Ca^{2+} channels per ribbon (~22 at −10 mV), either a sensor with different Ca^{2+} sensitivity and/or a different spatial distribution of Ca^{2+} channels could underlie the apparent higher Ca^{2+} efficiency of vesicle recruitment in VHC-I.

Voltage dependence of RRP exocytosis: functional organization of Ca^{2+} channels

The relationship between Δ_{Cm} and I_{Ca} was then studied when hair cells were step-depolarized to various membrane potentials from −90 mV to 5 mV at a constant 25 ms duration (Fig. 3*A*). This protocol mainly probed RRP exocytosis by varying

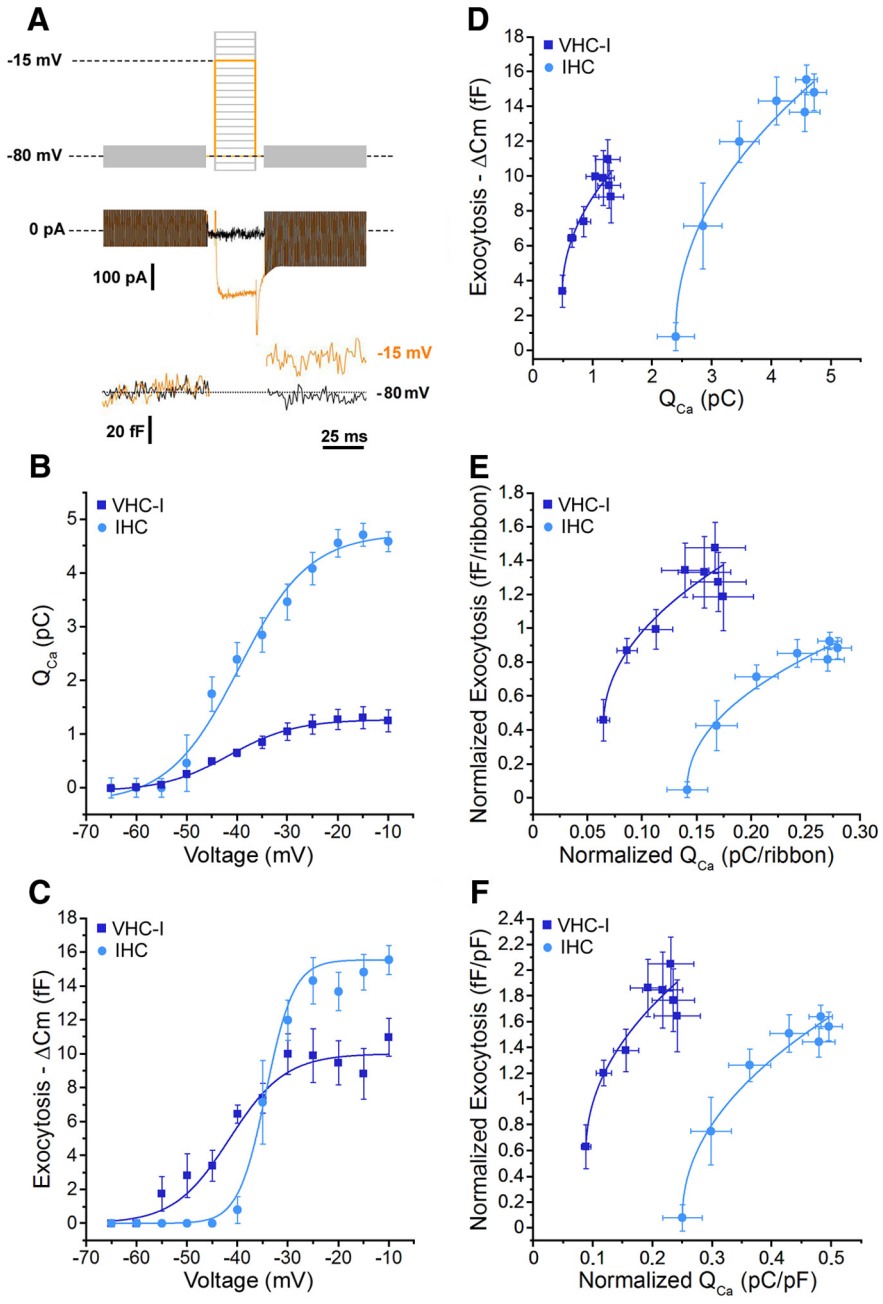

Figure 3. Voltage dependence of exocytosis in VHC-I and IHCs. ***A***, Cells were depolarized by voltage-steps from −90 mV to 5 mV in 5 mV increments for a constant 25 ms duration. Examples of I_{Ca} and capacitance measurements (Δ_{Cm}) in an IHCs are shown. ***B***, Q_{Ca} was plotted against membrane potential from −65 mV to −10 mV. Data were fit with a Boltzmann function with a $V_{1/2}$ of −47.8 ± 1.3 and −38.2 ± 2.0 mV in VHC-I ($n = 6$) and IHCs ($n = 8$), respectively. ***C***, Δ_{Cm} values were plotted against membrane potential. Data were fitted with a Boltzmann function with a $V_{1/2}$ of −42.5 ± 1.8 and −32.4 ± 0.5 mV in VHC-I ($n = 6$) and IHCs ($n = 8$), respectively. ***D***, Δ_{Cm} values plotted against Q_{Ca} were fitted with a power function and a power index of 0.61 and 0.49 in VHC-I ($n = 6$) and IHCs ($n = 8$), respectively. ***E***, Normalization to the number of ribbons. ***F***, Normalization to cell size (pF).

the open probability of Ca^{2+} channels in close vicinity to the Ca^{2+} sensor.

As with the ramp-protocol (Fig. 1*A*), I_{Ca} step-activation showed a different voltage dependence in VHC-I and IHCs (Fig. 3*B*). Indeed, the Q_{Ca} voltage dependence was best fitted by using a sigmoidal Boltzmann function with a $V_{1/2}$ of −47.76 ± 1.32 mV and −38.18 ± 2.00 mV in VHC-I ($n = 6$) and IHCs ($n = 8$), respectively ($p < 0.05$). Notably, the voltage dependence of Δ_{Cm} also indicated a different $V_{1/2}$ of −42.51 ± 1.79 mV and −32.42 ± 0.55 mV in VHC-I and IHCs, respectively ($p < 0.05$; Fig. 3*C*). The slope of the Boltzmann function indicated a much steeper voltage dependence in IHCs exocytosis than in VHC-I (5.07 ± 1.79 fF/mV and 2.16 ± 0.19 fF/mV, respectively; $p < 0.05$). These data suggested that a significant exocytosis can occur at more negative voltage in VHC-I (threshold close to −60 mV) compared with IHCs (threshold close to −50 mV). Notably, auditory hair cells of the amphibian papilla also display Ca^{2+} current with an activation threshold in the −70 mV range (Graydon et al., 2011). These results suggest that the Ca^{2+} channels of some hair cells have unusual properties. On the other hand, the voltage exocytotic threshold values of VHC-I fit well with the more negative resting membrane potential in VHC-I (Rüsch et al., 1998; Brichta et al., 2002) (∼−70 mV) than in IHCs (∼−55 mV) (Johnson et al., 2011). The steeper voltage dependence of exocytosis in IHCs suggested a higher sensitivity to voltage change in auditory hair cell ribbon synapses than in VHC-I synapses.

The relationship between Δ_{Cm} and Q_{Ca} could be fitted with similar power functions in VHC-I and in IHCs: with a low-power index $a = 0.61$ and 0.49 and a slope A (Ca^{2+} efficiency) = 7.04 ± 1.39 fF/pC and 9.81 ± 1.22 fF/pC ($p = 0.23$), respectively (Fig. 3*D*). A similar Ca^{2+} efficiency suggests that exocytosis is similarly related to the open probability of Ca^{2+} channels in both types of hair cells. The nearly linear behavior is compatible with an organization of independent Ca^{2+} nanodomains whose activities are linearly summing up with voltage. In these nanodomains, the activity of one or few Ca^{2+} channels (here probably 3) is sufficient to activate the release of a nearby vesicle (Brandt et al., 2005). In addition, the quasi-linear Ca^{2+}-dependency of exocytosis, when evoked by the activation of voltage-gated Ca^{2+} channels, has been proposed to result from the summation of the activity of several supralinear ribbons with different Ca^{2+} sensitivities (Heil and Neubauer, 2010).

Q_{Ca} thresholds were significantly lower in VHC-I than in IHCs (0.49 ± 0.04 pC and 2.33 ± 0.16 pC, respectively, $p < 0.05$). Furthermore, the Q_{Ca} dynamic range covered by VHC-I was much smaller than in IHCs (1.0 ± 0.22 pC and 2.19 ± 0.14 pC, respectively; $p < 0.05$). When normalized to the number of ribbons per cell, the relationship between Δ_{Cm} and Q_{Ca} showed a similar Ca^{2+} efficiency of 3.32 ± 1.24 fF/pC and 2.44 ± 0.35 fF/pC in VHC-I and IHCs, respectively; $p = 0.58$ (Fig. 3*E*). The Q_{Ca} thresholds per ribbon were estimated to be 0.066 ± 0.005 pC and 0.14 ± 0.01 pC in VHC-I and IHCs, respectively ($p < 0.05$). The Q_{Ca} dynamic range per ribbon was 0.10 ± 0.01 pC in VHC-I and 0.15 ± 0.02

pC in IHCs, ($p < 0.05$). Similar results were found when normalizing to cell size (Fig. 3*F*). Again, the difference in Q_{Ca} threshold and Q_{Ca} dynamic range in VHC-I and IHCs could be explained either by a different Ca^{2+} sensitivity of the Ca^{2+} sensor and/or a different organization–regulation of Ca^{2+} channels at the ribbon.

Spatial organization of Cav1.3 channels

Using fluorescence confocal imaging of immunolabeled whole-mount OC and utricles at P12–P14, we assessed the number of ribbons and distribution of Cav1.3 channels in hair cells (Figs. 1*E′* and 4). Ribbon synapses were identified as colocalized spots of ribbons (ribeye labeling with anti-CtBP2) and Cav1.3 labeling. As aforementioned in the manuscript, there were nearly twice as many ribbons in IHCs than in VHC-I (Fig. 1*E′*). However, when normalizing to cell membrane surface (C_m), a similar ribbon density of 1.40 ± 0.15 pF^{-1} and 1.79 ± 0.07 pF^{-1} ($p = 0.13$) was found in VHC-I and IHCs, respectively. Assuming a specific membrane capacitance of 0.01 pF/μm^2, we estimated the ribbon density to be 1.4 and 1.79 per 100 μm^2 in VHC-I and IHCs, respectively.

Imaris analysis of 3D stack reconstruction indicated that the ribbons had a similar size distribution in VHC-I and IHCs, with a mean volume of 0.038 ± 0.001 μm^3 ($n = 291$) and 0.033 ± 0.001 μm^3 ($n = 333$), respectively ($p = 0.90$; Fig. 4*E*). JaCoP analysis of the nearest neighbor distance distribution between ribbon synapses showed a similar mean distance of 1362 ± 88 nm and 1174 ± 58 nm in VHC-I and IHCs, respectively. The nearly constant distance between ribbons was similar to previous values reported in IHCs (Meyer et al., 2009). Interestingly, we found a greater heterogeneity in the size of the ribbon-associated Cav1.3 channel clusters in VHC-I than in IHCs. In VHC-I, Cav1.3 spots showed a 50/50 distribution in small- (0.056 ± 0.001 μm^2) and large-sized spots (0.209 ± 0.002 μm^2) (Fig. 4*F*). Cav1.3 spots in IHCs showed a single Gaussian distribution in size (0.194 ± 0.002 μm^2), a value not different from the larger VHC-I Cav1.3 spots ($p = 0.25$). The presence of a large proportion of smaller Cav1.3 spots in VHC-I, giving a global mean surface of 0.155 ± 0.004 μm^2 (i.e., a surface reduction of 20% compared with IHCs, is in good correlation with their smaller Ca^{2+} current density than in IHCs) (Fig. 1*A*). Considering a mean number of 158 and 110 Ca^{2+}

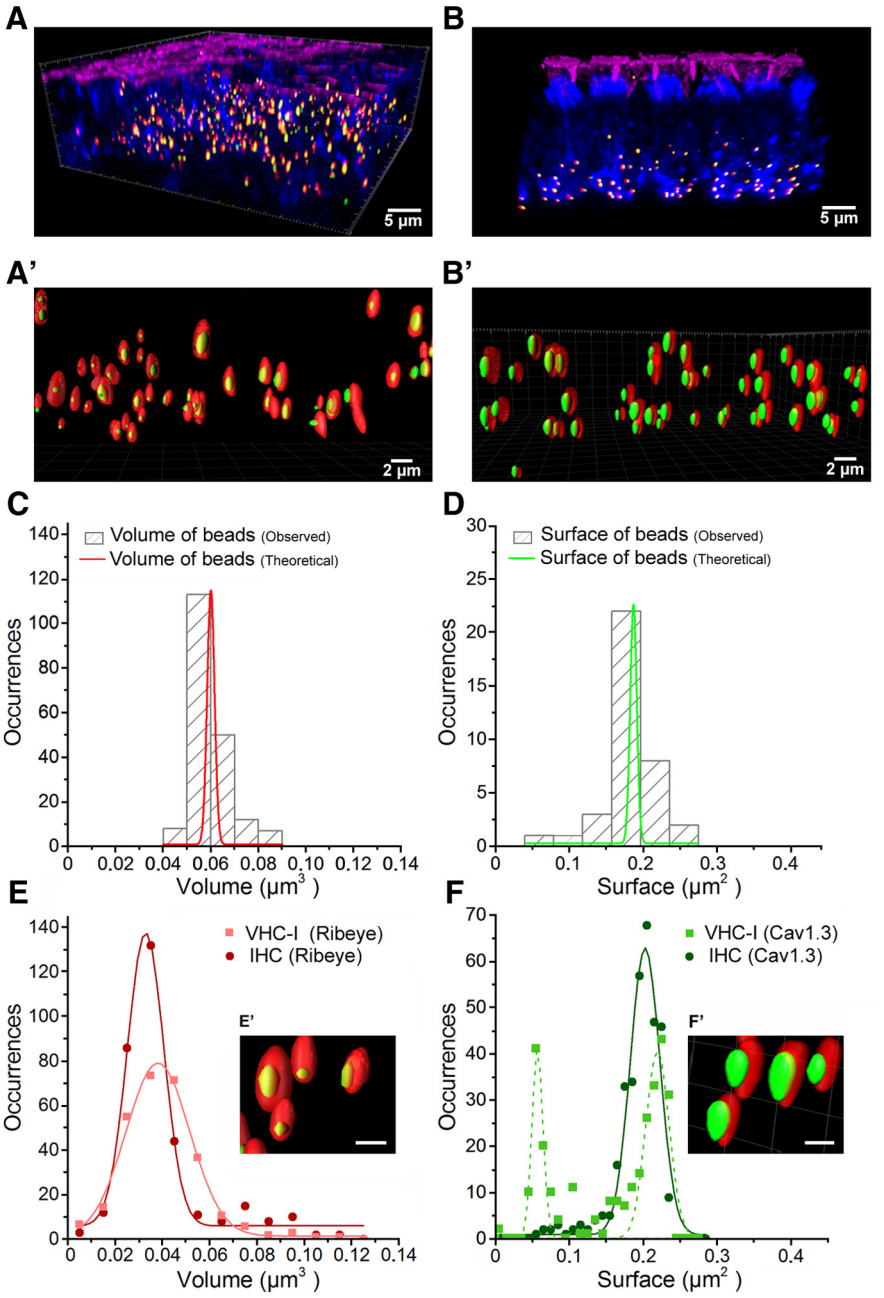

Figure 4. Spatial distribution of Cav1.3 channels in VHC-I and IHCs. ***A***, ***B***, 3D Imaris reconstructions of confocal images from the central striolar region of an utricle and the low-frequency apical turn of an OC, respectively. Both organs were dissected from mice at P14. Hair cells were stained for F-actin (phalloidin, pink), otoferlin (anti-otoferlin, blue), ribbons (anti-CtBP2, red), and Cav1.3 (anti-α 1D, green). ***A′***, ***B′***, 3D-reconstructed images at higher magnification of some ribbons and their associated Cav1.3 cluster in vestibular (***A′***; VHC-I) and cochlear hair cells (***B′***; IHCs). It is to be noted that these images are 3D stack reconstructions. The distance between ribbons as well as their size are here distorted in 2D representation. ***C***, Fluoresbrite YO carboxylate microspheres were taken as reference for the ribbon volume analysis (see Materials and Methods). The hatched gray bars represent the observed volume distribution of the beads (after correction for oblate and prolate image distortion) compared with their theoretical value (red). ***D***, Fluoresbrite Yellow Green microspheres were taken as references for the spheroid surface analysis of Cav1.3 clusters. Hatched gray bars represent the observed surface distribution of the bead surfaces compared with their theoretical value (green). ***E***, Volume distribution analysis of ribbons in VHC-I (light red, filled squares) and IHCs (dark red, filled circles) displayed no significant difference (VHC-I, 291 ribbons, 0.038 ± 0.001 μm^3; IHCs, 333 ribbons, 0.033 ± 0.001 μm^3, $p = 0.90$). ***F***, Surface distribution analysis of Cav1.3 clusters. In VHC-I, Cav1.3 channel clusters distributed in two equal populations of small (0.056 ± 0.001 μm^2) and large (0.209 ± 0.002 μm^2) clusters (green dashed line). In IHCs, the distribution of Cav1.3 channel clusters was fitted with a simple Gaussian (0.194 ± 0.002 μm^2; dark green). ***E′***, ***F′***, Insets, Synaptic ribbons at high magnifications in one VHC-I (***E′***) and one IHC (***F′***). Scale bar, 1 μm.

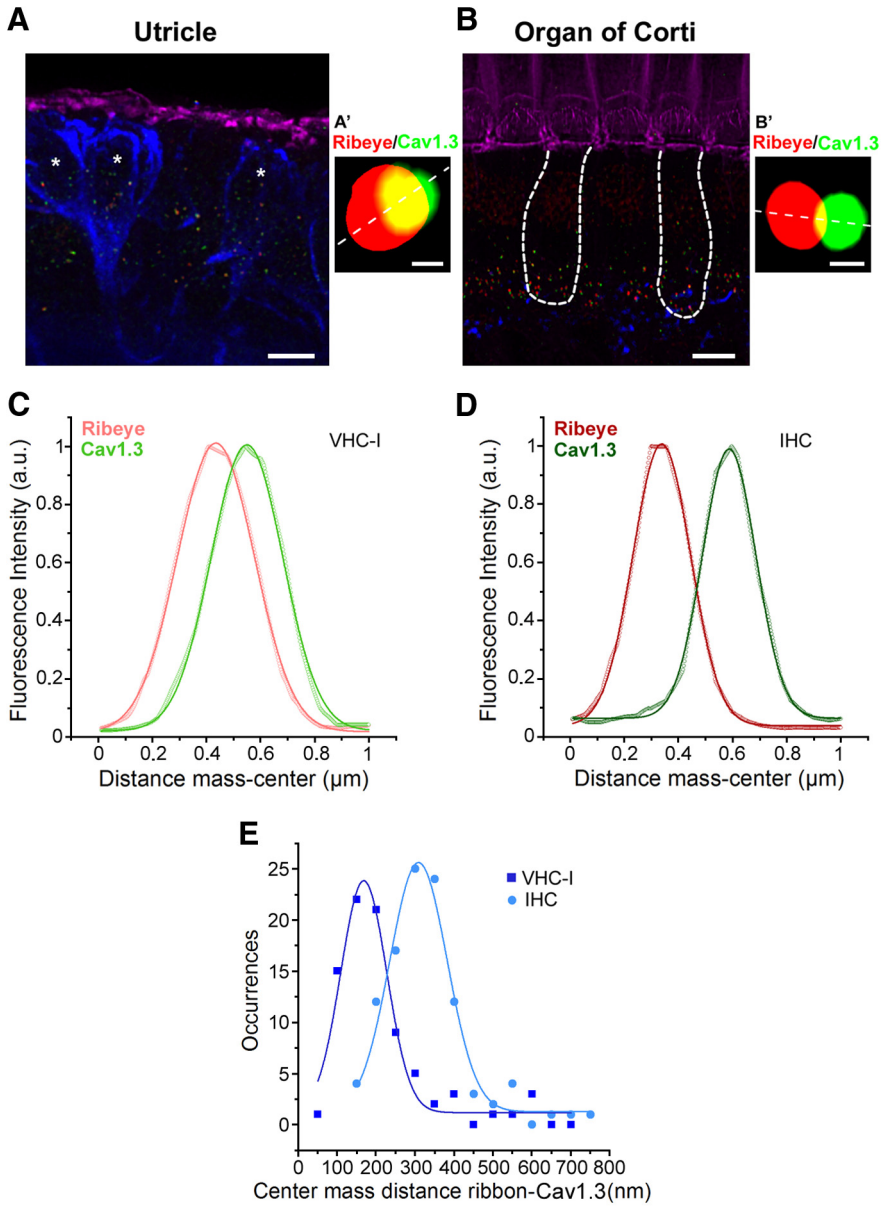

Figure 5. Colocalization between Cav1.3 channels and ribbons. ***A***, ***B***, 3D stack reconstruction of confocal images of utricle (***A***, striolar region) and OC (apical region, ***B***). Organs (P14) were labeled for F-actin (pink), Cav1.3 (green), and CtBP2 (red ribbons). Afferent fibers were labeled with Anti-NF200 (blue). Asterisks indicate VHC-I surrounded by large calyceal nerve terminals. Scale bar, 6 μm. An example of a Cav1.3 channel cluster (green) and its ribbon (red) is shown for VHC-I (***A'***) and IHCs (***B'***). Scale bar, 0.25 μm. ***C***, ***D***, Colocalization between Cav1.3 and ribbon (CtBP2-ribeye) was assessed by plotting the fluorescence intensity profile from a line scan (***A'***, ***B'***, white dashed line). An example of fluorescence intensity profile is shown for VHC-I (***C***) and IHCs (***D***). ***E***, Colocalization analysis using JACoP plugin in ImageJ. Gaussian fit of the occurrences of center mass distance measured between ribbon and Cav1.3 VHC-I (167.77 ± 4.53 nm, $n = 83$) and IHCs (308.34 ± 4.68 nm, $n = 106$) suggested a tighter organization of Cav1.3 channels and ribbons in VHC-I.

channels per ribbon (with an homogenous Ca^{2+} channel distribution between ribbons), we estimated a mean density of 1019 and 567 Ca^{2+} channels per μm^2 in VHC-I and IHCs active zones, respectively.

Next, we performed a 3D colocalization analysis of Cav1.3 and CtBP2 fluorescent spots using JACoP software. The center mass distances between Cav1.3 and CtBP2 (ribbons) spots were smaller in VHC-I than in IHCs (167.8 ± 4.5 nm, $n = 83$ ribbons; and 308.4 ± 4.5 nm, $n = 106$ ribbons; $p < 0.05$; Figure 5). 3D Imaris analysis indicated that 39.5 ± 4.0% of the Cav1.3 surface area did not overlap with CtBP2 in IHCs, whereas the figure was only 3.5 ± 3.0% in VHC-I. This difference in the center mass distance may reflect a different ribbon morphology with a more elongated ellipsoid form in IHCs compared with VHC-I. It may also be due to a different arrangement of Ca^{2+} channels at the ribbons. However, our optical analysis is hindered by the spatial resolution of confocal microscopy, which is limited to a lateral resolution (R) of ~130–150 nm ($r = 0.37\ \lambda_{ex}/NA$).

To further probe the organization of Cav1.3 channels at a higher spatial resolution we then used STED microscopy in P21 VHC-I and P21 IHCs (Fig. 6). Cav1.3 channels were found to form ellipsoidal patches below the ribbons in IHCs, with semi-major axis (a) of 190 ± 32 nm and semi-minor axis (b) of 86 ± 9 nm, giving a mean surface area (S) of 0.051 ± 0.003 μm^2. In VHC-I, Cav1.3 channel clusters formed more spherical patches with a = 128 ± 22 nm and b = 110 ± 20 nm, giving S = 0.042 ± 0.003 μm^2 ($p = 0.45$; non-significantly different with the S of IHCs Cav1.3 clusters; Fig. 6*E*). If we consider that Cav1.3 channels are regularly targeted to the periphery of the ellipse, an elongated ellipse in IHCs predicts that the focus points of interaction of Ca^{2+} channels ($F = \sqrt{a^2 - b^2}$) are more distant in IHCs ($F = 168 \pm 37$ nm, $n = 15$) than in VHC-I ($F = 60 \pm 30$ nm, $n = 21$; $p < 0.05$; Fig. 6*F*). In this model, Ca^{2+} influx from individual channels more efficiently sums up below VHC-I ribbons than in IHCs.

Unlike confocal microcopy performed in P14 VHC-I (Fig. 4), the surface area distribution of Cav1.3 patches is distributed in a single Gaussian in P21 VHC-I (Fig. 6*E*). The surface areas of the Ca^{2+} channels clusters measured with STED microscopy were found somewhat smaller in both types of hair cells compared with the less resolutive confocal microscopy (Fig. 4). The density of Ca^{2+} channels was then estimated here using STED microscopy to be ~3500 and 2150 Ca^{2+} channels/μm^2 in P21-VHC-I and P21-IHCs, respectively.

Probing the coupling between Ca^{2+} channels and sensors with exogenous Ca^{2+} chelators

The physical distance between Cav1.3 channels and Ca^{2+} release sensors was estimated by analyzing the concentration dependence of intracellular BAPTA and EGTA on hair cell exocytosis (Fig. 7). A similar method has been used to address the same issue in several central synapses (Eggermann et al., 2011). Here, we tested the effects of various concentrations of EGTA and BAPTA on exocytosis ($\Delta C_m/Q_{Ca}$) evoked by a 25 ms voltage step depo-

larization from −80 mV to −10 mV. We found that the fast Ca^{2+} chelator, BAPTA, completely suppressed exocytosis with half-maximal inhibitory concentrations (K_i) of 1.2 ± 0.2 mM and 0.7 ± 0.2 mM in VHC-I and IHCs, respectively. Comparable Ki values for BAPTA were reported in gerbil apical and basal IHCs (Johnson et al., 2008). On the other hand, the slow Ca^{2+} chelator, EGTA, only partly reduced exocytosis with a K_i of 9.0 ± 0.7 and 2.6 ± 0.9 mM in VHC-I and IHCs, respectively ($p < 0.05$; Fig. 7). The lower sensitivity to EGTA in VHC-I argues in favor of a tighter coupling organization between Ca^{2+} channels and release sensors compared with IHCs. To evaluate the coupling distance between Ca^{2+} channels and release sites, data for EGTA were fit by a model of Ca^{2+} diffusion and buffering (Bucurenciu et al., 2008; Vyleta and Jonas, 2014) (see Materials and Methods). A mean coupling distance of 72 ± 20 nm and 46 ± 12 nm was estimated in IHCs and VHC-I, respectively ($p < 0.05$). It is likely that this coupling distance, evaluated here for a 25 ms step-depolarization during which Ca^{2+} has time to diffuse over several hundreds of nm, could rather reflect the mean distance of overlapping individual Ca^{2+} nanodomains than the coupling distance between Ca^{2+} channels and sensors (Kim et al., 2013). A looser organization of Ca^{2+} channels in IHCs may in part explain the apparent lower Ca^{2+} sensitivity of exocytosis when considering the global Ca^{2+} current in Figure 3. A loose coupling organization of Ca^{2+} channels in IHCs would enable endogenous Ca^{2+} buffers to more efficiently control saturation of the sensors. This would likely allow a more gradual Ca^{2+}-evoked exocytosis in IHCs than in VHC-I and therefore explain the remarkable large dynamic range (up to 40 dB) of sound-evoked discharge rates of individual auditory nerve fibers (Kiang, 1965; Taberner and Liberman, 2005).

Mouse IHCs and VHC-I exocytosis were here recorded at the onset of cochlear and vestibular potentials, an age at which hair cells are not yet fully mature. However, our conclusions likely also apply to adult hair cells because their fundamental exocytotic properties (rate and calcium dependence) remain largely unchanged after postonset development, as demonstrated in mature IHCs (Johnson et al., 2005; Beurg et al., 2010; Wong et al., 2014) (>P20–P25). Furthermore, the STED imaging microscopy experiments in our study were carried out at P21, an age at which VHC-I and IHCs can be considered nearly mature.

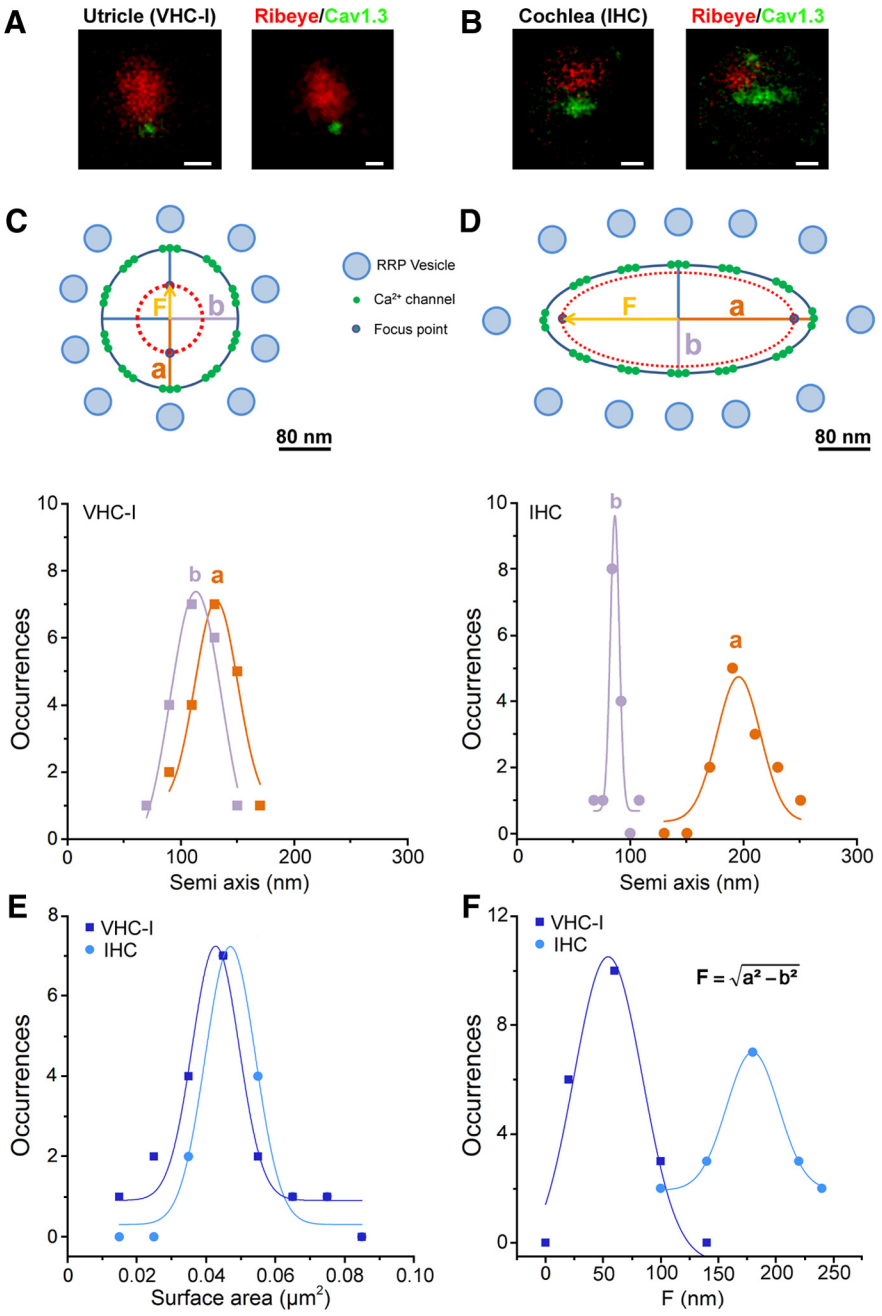

Figure 6. Ca^{2+} channel organization in VHC-I and IHCs by STED microscopy. ***A***, ***B***, Two examples of STED images of immunolabeled ribbon (anti-CtBP2, red) and Ca^{2+}-channel (anti-Cav1.3 green) in P21 VHC-I (***A***) and P21 IHCs (***B***). Scale bars, 200 nm. ***C***, ***D***, Semiaxis (a, b) size distribution in VHC-I (***C***) and IHCs (***D***). Data points were fitted by a simple Gaussian. The long semi axis "a" and short semi-axis "b" are of similar values in VHC-I (***C***), whereas they show a nearly 2 times difference in IHCs (***D***). This suggested that the arrangement of the Ca^{2+} channels clusters at the ribbon membrane forms an elongated stripe-like ellipsoide in IHCs and a nearly circular disk in VHC-I. ***C***, ***D***, Top, Schematic representation of the active zone below the ribbon in VHC-I and IHCs. Assuming that the Ca^{2+} channels are uniformly distributed at the edge of the ellipse, an elongated ellipsoid distribution would give a larger distance for the interacting focus points of Ca^{2+} influx in IHCs compared with VHC-I. "F" represents the distance between the center of the ellipse and each focus point. The model assumes that Ca^{2+} channels are organized as individual nanodoamains for brief low-voltage stimulation (near threshold) and as microdomains with linear summation of Ca^{2+} activity for long high-voltage stimulations. This summation of Ca^{2+} influx would be more efficient in VHC-I than in IHCs. ***E***, Similar mean surface distribution of Cav1.3 clusters in VHC-I and IHCs. ***F***, Distribution and Gaussian fit of the distance between focus points and the center of the ellipse ("F") in VHC-I ("F" = 54.4 ± 5.9 nm) and IHCs ("F" = 179.9 ± 0.9 nm).

Determination of Ca^{2+} sensitivity of exocytosis by gradual Ca^{2+} uncaging

Exposure to 13 sequential low-intensity UV flashes, 200 ms apart, allowed a progressive step-increase in $[Ca^{2+}]_i$ and C_m in both

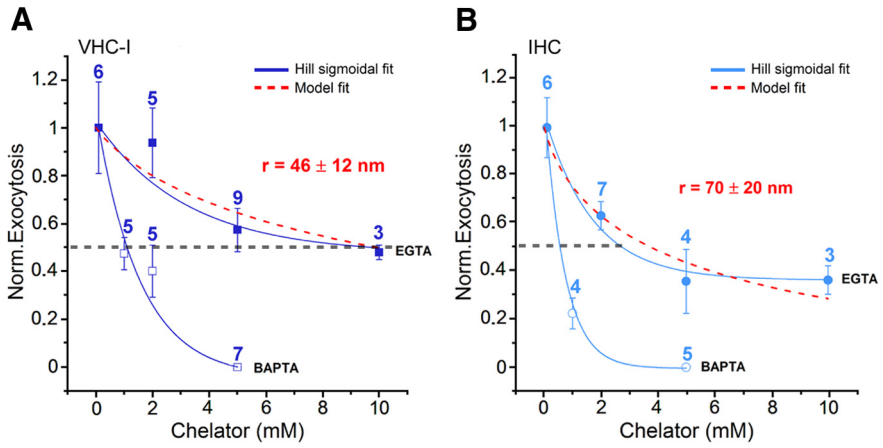

Figure 7. Concentration dependence of exogenous Ca^{2+} chelators. Ca^{2+} efficiency of exocytosis (Δ_{Cm}/Q_{Ca} obtained for a 25 ms depolarization from −80 mV to −10 mV) normalized to the maximum Ca^{2+} efficiency (obtained with 0.1 mM BAPTA) as a function of different concentrations of intracellular BAPTA and EGTA in VHC-I (***A***) and IHCs (***B***). The dotted red curves fit EGTA data using the linearized reaction diffusion equations of Ca^{2+} described in Materials and Methods. Best fits were obtained with a mean coupling distance between Ca^{2+} channels and sensors r of 46 ± 12 nm (***A***, VHC-I) and 70 ± 20 nm (***B***, IHCs). Solid lines indicate the fit with a Hill sigmoidal function. It is important to note that this coupling distance r was obtained for a somewhat long 25 ms depolarization at maximal channel open probability. It may likely reflect here the interacting coupling distance between individual Ca^{2+} nanodomains described in Figure 6.

VHC-I and IHCs loaded with DM-nitrophen (Fig. 8). A significant C_m jump began at the fifth flash and reached a similar maximal plateau at 206.27 ± 34.31 fF/pF and 233.42 ± 48.89 fF/pF (normalized to cell capacitance) in VHC-I and IHCs, respectively ($p = 0.3$). After each flash, the kinetics of Δ_{Cm} could be decomposed in a fast component that could be attributed to the RRP and a secondary slow component (SRP) that reflects the replenishment of the fusion sites by distant vesicles (Beutner et al., 2001). Similar experiments in *Otof* $^{-/-}$ VHC-I and *Otof*$^{-/-}$ IHCs, lacking otoferlin, gave a similar step-increase in $[Ca^{2+}]_i$ (Fig. 8*C*,*D*) but only a weak Δ_{Cm} response reaching a maximum of 12.71 ± 3.20 fF/pF and 2.25 ± 2.36 fF/pF in VHC-I and IHCs, respectively (Fig. 8*E*,*F*). These results confirmed that otoferlin is essential for efficient fast exocytosis in both VHC-I and IHCs (Roux et al., 2006; Dulon et al., 2009).

To determine the affinity of the Ca^{2+} sensor, each Δ_{Cm} plateau value was plotted against the corresponding $[Ca^{2+}]_i$ in both VHC-I and IHCs (Fig. 9*A*,*B*). Data were fitted using a similar Hill sigmoidal function with a K_D of 3.27 ± 0.59 μM and 4.05 ± 0.72 μM in control VHC-I and IHCs, respectively ($p = 0.46$). A similar cooperative Hill coefficient of 3.19 ± 0.69 and 2.69 ± 0.25, respectively, was found in VHC-I and IHCs ($p = 0.19$). The instantaneous-rate of the first exocytotic component (RRP), as estimated by linearly fitting the first 10–20 ms of the Δ_{Cm} jump, was also plotted against the various $[Ca^{2+}]_i$ obtained at each UV flash (Fig. 9*C*). Instantaneous rates were also fitted using a similar Hill sigmoidal function with a K_D of 1.28 ± 0.34 μM and 1.10 ± 0.24 μM in VHC-I and IHCs, respectively ($p = 0.9$). A similar cooperative Hill coefficient of 3.73 ± 0.67 and 4.12 ± 0.62 was found in VHC-I and IHCs, respectively ($p = 0.5$).

We then estimated the rate of the SRP by linearly fitting the first 50 ms after the deflecting point of the Δ_{Cm} response at each UV flash (Fig. 9*D*′, inset, black arrowhead). Plotted against the various $[Ca^{2+}]_i$ (Fig. 9*D*), the SRP rates could also be fitted using a sigmoidal Hill function with a K_D of 3.58 ± 0.27 μM and 1.03 ± 0.10 μM in VHC-I and IHCs, respectively ($p < 0.05$). The SRP rates against $[Ca^{2+}]_i$ showed a similar cooperative Hill coefficient of 4.22 ± 0.76 and 3.58 ± 0.54 in VHC-I and IHCs, respectively ($p = 0.56$). Considering that 94%–98% of the Δ_{Cm} response is abolished in *Otof*$^{-/-}$ VHC-I and *Otof*$^{-/-}$ IHCs (Fig. 9*A*,*B*), our results suggested that otoferlin has a Ca^{2+} affinity in the low micromolar range.

Surprisingly, previous Ca^{2+} uncaging experiments using a single high-intensity UV flash showed that the exocytotic rate of IHCs does not saturate even at high $[Ca^{2+}]_i$, such as 100 μM, rendering difficult to estimate the K_D value (Beutner et al., 2001; Neef et al., 2014). When using a single high-power intensity UV flash and various concentrations of intracellular DM-nitrophen (2.5, 4, and 10 mM) and Ca^{2+} (5 and 10 mM), we also observed a similar apparent nonsaturating exocytotic rate in both VHC-I and IHCs when varying $[Ca^{2+}]_i$ from 1 to 80 μM (data not shown). The discrepancy between results using the multiflash and the single flash protocol could be explained by the following observations. Indeed, we found that stepping the membrane potential from a holding potential of −70 mV to −30 mV for 500 ms (near $V_{1/2}$ of I_{Ca}) before a single flash photolysis led to faster release rates and larger RRP exocytosis in IHCs (without prestep: rate constant = 5.93 ± 0.70 s^{-1} and plateau ΔC_m = 11.02 ± 2.33 fF/ribbon and with a prestep, rate constant = 14.51 ± 3.97 s^{-1} and plateau ΔC_m = 20.36 ± 3.21 fF/ribbon, $p < 0.05$; data not shown).

The abovementioned observations suggest that holding the hair cells at a low negative potential of −70 mV possibly impeded the functional Ca^{2+} environment of the release sites. It is tempting to speculate that a significant Ca^{2+} channel activity is required to maintain a high density of vesicles at the active zone. Indeed, Ca^{2+}-dependent synaptic vesicle trafficking, leading to a superlinear exocytotic component varying with Ca^{2+} load (Schnee et al., 2011), has been suggested in hair cells (Cho et al., 2011; Levic et al., 2011). Our multiflash protocol, increasing [free $Ca^{2+}]_i$ by steps in the same cell, likely offers the advantage of progressively charging the sites of release with vesicles during the sequential UV flashes. It is possible that a single high energy UV flash from vesicle-depressed ribbons would simultaneously test replenishment and fusion, thereby explaining the nonsaturating exocytotic responses (Beutner et al., 2001). Alternatively, it is possible that part of the nonsaturating exocytotic response, when a single high energy photolysis is used, comes from a Ca^{2+}-independent osmotic-pressure effect on vesicle fusion because DM-nitrophen molecules undergo cleavage to yield two products with Ca^{2+} and H^+ release (Ellis-Davies et al., 1996).

Similarly to Beutner et al. (2001), we found that the maximal instantaneous release rates were more than one order of magnitude higher when using the uncaging Ca^{2+} protocol compared with the RRP kinetics experiments with voltage activation of Ca^{2+} channels in Figure 1*C* (VHC-I: 10.82 ± 2.40 pF/s vs 0.57 ± 0.23 pF/s; IHCs: 11.50 ± 3.60 pF/s vs 0.50 ± 0.09 pF/s, respectively). Considering that vesicle fusion occurs exclusively at the ribbon active zone and that $[Ca^{2+}]_i$ rise uniformly in the hair cells during the uncaging experiments, one can speculate that an elevation of $[Ca^{2+}]_i$ at large distance from the active zone greatly influences the rate of vesicle fusion. In other words, the pressure

of the Ca^{2+}-dependent supply of vesicle controls the rate of fusion at the ribbon active zone. It is worth recalling that during the depolarizing-RRP protocol, the Ca^{2+} microdomain remains relatively small with a decreasing $[Ca^{2+}]_i$ gradient ranging from 80 μM at ~10 nm from the Ca^{2+} channels to ~10 μM at ~1.4 μm (Wu et al., 1996). Alternatively or in addition, during the Ca^{2+} uncaging protocols, we cannot exclude the participation of a large extra-ribbon vesicle fusion that speeds up the release rate in both types of hair cells.

Endocytosis kinetics and Ca^{2+} dependence

Remarkably, during the multiflash protocol, the instantaneous rate of exocytosis decreased strongly at $[Ca^{2+}]_i$ >8 μM in both types of hair cells (Fig. 8*E*,*F*). Considering that a 200 ms period between each stimulation is sufficient to limit vesicle depression (Levic et al., 2011), we speculated that the decrease in Δ_{Cm} responses was essentially due to a progressive increase in the endocytotic rate when $[Ca^{2+}]_i$ rises >8 μM. Fast endocytosis of vesicle has indeed been shown to be triggered during a transient rise in $[Ca^{2+}]_i$ in many cell types (Beutner et al., 2001; Van Hook and Thoreson, 2012; Wu and Wu, 2014). The fit of our data with a sigmoidal function gave a K_D of 7.36 ± 0.84 μM and 9.79 ± 1.79 μM in VHC-I and IHCs, respectively (p = 0.35; Fig. 9*E*). These results suggested that vesicle endocytosis displays a similar high Ca^{2+} sensitivity in VHC-I and IHCs.

The rate of endocytosis was also studied when applying a single high-energy UV flash in both VHC-I and IHCs loaded with an internal solution with 10 mM DM-nitrophen and 10 mM Ca^{2+}. The $[Ca^{2+}]_i$ was estimated to instantaneously reach a value close to 80 μM as measured with the low affinity Ca^{2+} dye Fluo-5N (K_D = 90 μM; data not shown). This Ca^{2+} uncaging protocol triggered a fast Δ_{Cm} response peaking within 200 ms and reaching a maximum value of 544 ± 22 fF and 697 ± 60 fF in VHC-I and IHCs, respectively (Fig. 10*A*,*B*). The exocytotic phase was then followed by a fast decline in C_m that could be due to endocytotic membrane retrieval as previously described (Beutner et al., 2001). We found that endocytosis displayed an apparent slower instantaneous rate in VHC-I than in IHCs (0.18 ± 0.04 pf/s and 1.01 ± 0.14 pf/s, respectively, p < 0.001; Fig. 10*C*). However, when normalized to the amplitude of the endocytotic peak, the kinetics of endocytosis showed similar time constants in VHC-I and IHCs (1.47 ± 0.42 s^{-1} and 3.10 ± 0.69 s^{-1}, respectively, p = 0.051; Fig. 10*D*). *Otof* $^{-/-}$ VHC-I and *Otof* $^{-/-}$ IHCs, displaying a reduced exocytotic response, showed apparent slower instantaneous rates than their respective controls (0.05 ± 0.01 pf/s and 0.24 ± 0.09 pf/s, respectively; p < 0.05).

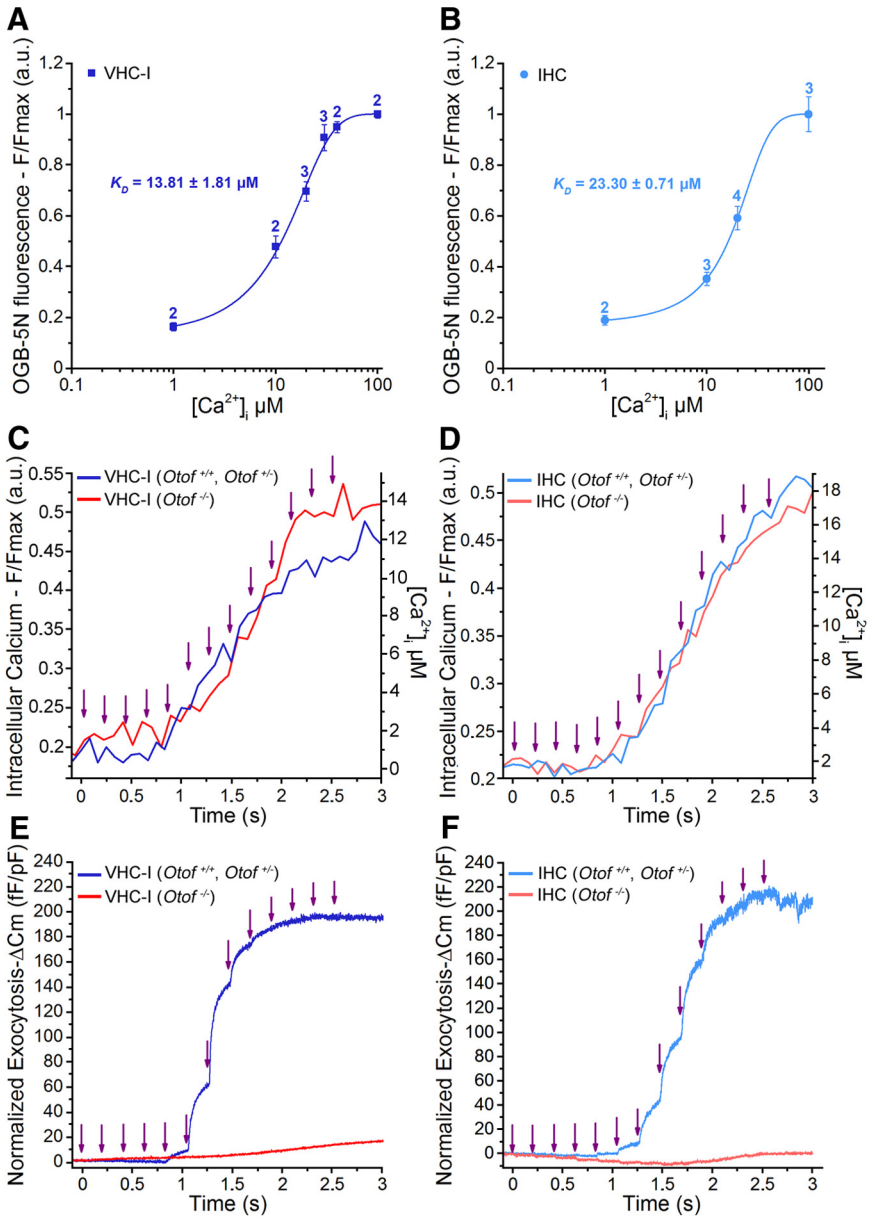

Figure 8. Step increase in $[Ca^{2+}]_i$ and exocytosis evoked by multiflash Ca^{2+} uncaging. ***A***, ***B***, *In vivo* calibration of the calcium dye OGB-5N in VHC-I (***A***) and IHCs (***B***) gave a dissociation constant close to the theoretical value of 20 μM (13.81 μM VHC-I and 23.30 μM IHCs). Numbers above each data point indicate the number of cells. ***C–F***, Simultaneous recording of $[Ca^{2+}]_i$ (F/F_{max}) and Δ_{Cm} (normalized to cell size) during the multiflash protocol (purple arrow indicates each UV flash) in VHC-I (***C***, ***E***) and IHCs (***D***, ***F***). Control VHC-I (dark blue line, mean of n = 7) and *Otof* $^{-/-}$ VHC-I (red line, mean of n = 10); control IHCs (light blue, mean of n = 9) and *Otof* $^{-/-}$ IHCs (red line, mean of n = 7).

However, when normalized to the endocytotic peak amplitude, the endocytotic kinetics of *Otof* $^{-/-}$ VHC-I and *Otof* $^{-/-}$ IHCs showed similar time constants to those of controls (VHC-I, 1.47 ± 0.42 s^{-1} and 0.51 ± 0.13 s^{-1}, p = 0.37; IHCs, 3.10 ± 0.69 s^{-1} and 2.41 ± 0.60 s^{-1}; p = 0.55; respectively for controls and *Otof* $^{-/-}$). Furthermore, VHC-I and IHCs lacking otoferlin displayed a similar percentage of membrane retrieval (control VHC-I: n = 7, 35.52 ± 14.26%, *Otof* $^{-/-}$ VHC-I, n = 7, 40.26 ± 8.93; p = 0.8; control IHCs: n = 13, 52.95 ± 4.43%, KO IHCs, n = 7, 33.09 ± 13.34%; p = 0.08; Fig. 10*E*). These results suggested that otoferlin is not essential for the fast endocytotic process in both VHC-I and IHCs, in agreement with Neef et al. (2014).

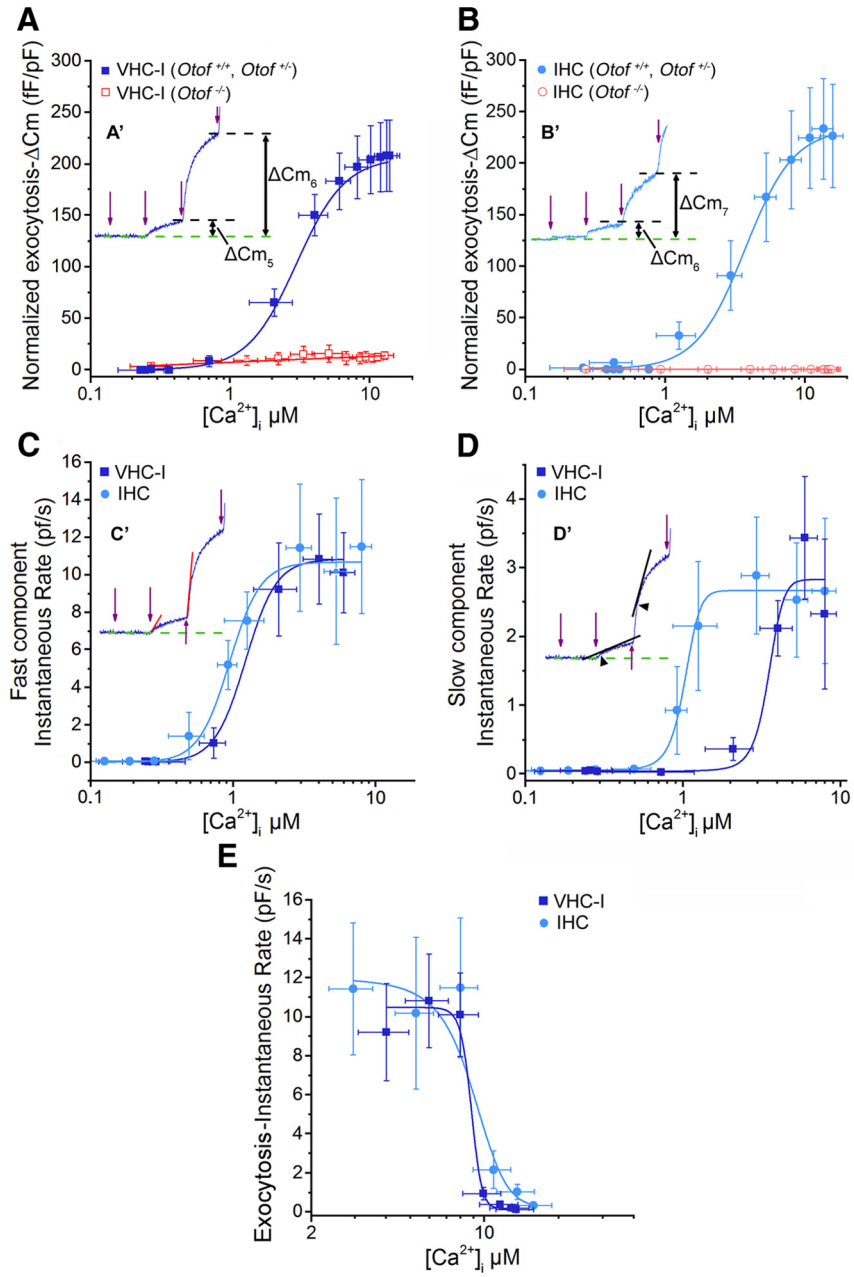

Figure 9. Determination of Ca^{2+} sensitivity of exocytosis in VHC-I and IHCs. ***A***, ***B***, From the experiments of Figure 8, mean Δ_{Cm} responses at each UV flash were plotted against corresponding $[Ca^{2+}]_i$ for VHC-I (***A***) and IHCs (***B***). ***A'***, ***B'***, Insets, Δ_{Cm} after two UV flashes (fifth flash: Δ_{Cm5} and sixth flash: Δ_{Cm6}) in control mice. Δ_{Cm} responses in *Otof* $^{-/-}$ VHC-I and *Otof* $^{-/-}$ IHCs show a very poor Ca^{2+} dependence (red lines). ***A'***, ***B'***, The black dashed lines indicate the Δ_{Cm} plateau after each UV flash. Data points were fitted with a Hill sigmoidal function. ***C***, The instantaneous rate of the Δ_{Cm} fast component after each UV flash was plotted against $[Ca^{2+}]_i$ for VHC-I (dark blue) and IHCs (light blue). ***C'***, Inset, The method used to measure the instantaneous rate of the fast component. We used a linear function to fit the first 20 ms of the capacitance response (red lines). As in ***A*** and ***B***, we used a Hill sigmoidal function to fit these data points. ***D***, The second slow component of the Δ_{Cm} response was also plotted against $[Ca^{2+}]_i$. ***D'***, Inset, The method used. We linearly fitted the first 50 ms (black lines) after the deflection point of the response (arrowhead). Data points were fit with a Hill sigmoidal function. ***E***, The instantaneous rate of the fast Δ_{Cm} responses deeply decreased at $[Ca^{2+}]_i$ >8 μM. Data points were fitted with a decreasing sigmoidal function to obtain K_i (constant of inhibition) of exocytosis, which we considered as the K_D for endocytosis.

Discussion

We found that VHC-I and IHC ribbon synapses share several common structural and functional properties: (1) a similar density of ribbons (relative to cell membrane surface) as well as a similar ribbon size and interdistance interval distribution; (2) an otoferlin-dependent exocytosis with similar high intrinsic Ca^{2+} sensitivity; and (3) an otoferlin-independent endocytosis with similar kinetics and Ca^{2+} dependence. Conversely, we found fundamental differences that essentially concern the functional organization of Ca^{2+} channels: (1) the Ca^{2+} channel density; (2) the voltage dependence of Ca^{2+}-currents and exocytosis; and (3) the spatial organization of Cav1.3 channels at the ribbons.

The synaptic ribbons

First described by Smith and Sjostrand (1961), these electron-dense bodies, to which hundreds of synaptic vesicles aggregate, are thought to be the main sites where conventional synaptic chemical transmission occurs in hair cells. At the ultrastructural level, VHC-I ribbons have been described to have a spheroid form (Wersäll et al., 1967; Favre and Sans, 1979), whereas IHC ribbons display an elongated plate-like form (Sobkowicz et al., 1982). The IHC ribbons facing high-spontaneous rate fibers tend to be shorter and rounder than those facing low-spontaneous rate fibers but have a similar overall volume (Kantardzhieva et al., 2013). Our study showed that mouse VHC-I and IHC ribbons display a similar volume distribution, suggesting that a similar number of vesicles are attached to them. This hypothesis was reinforced by our findings that the RRP per ribbon in both VHC-I and IHCs is of similar size. These results are consistent with previous ultrastructural studies showing a rather constant density of vesicles tethered to the ribbons whatever the type of hair cells, such as frog vestibular hair cells (Lenzi et al., 1999), turtle auditory hair cells (Schnee et al., 2005), and cat IHCs (Kantardzhieva et al., 2013).

An intriguing finding was that VHC-I and IHCs display a similar ribbon density (relative to cell membrane surface), suggesting that the hair cell rather than the morphology of the postsynaptic nerve fiber determines the occurrence and the distribution of each ribbon. Furthermore, the 3D interdistance between ribbons was similar in both types of hair cells (i.e., 1.2–1.4 μm), suggesting that each ribbon tends to regulate the occurrence of other ribbons in its vicinity. A similar distribution of the nearest neighboring distance between ribbons has been reported in high- and low-frequency mouse IHCs (Meyer et al., 2009).

Ca^{2+} sensitivity of otoferlin-dependent exocytosis

Our multistep Ca^{2+} uncaging experiments showed that otoferlin-dependent exocytosis in VHC-I and IHCs displays a comparable high Ca^{2+} sensitivity with K_D within the micromolar

range between 1 and 4 μM. In addition, both cell types exhibit a similar Ca^{2+} cooperativity with a Hill coefficient between 3 and 4. These results are in good agreement with the data of Johnson and Chapman (2010) showing that, *in vitro*, otoferlin C2 domains accelerate fusion of liposomes bearing SNARE with high Ca^{2+} affinity with a K_D near 2 μM. This apparent Ca^{2+} affinity of otoferlin is nearly one order of magnitude greater than that reported for synaptotagmin I (Brose et al., 1992; Davis et al., 1999). Notably, synaptotagmin I is transiently expressed in immature spiking IHCs before the onset of hearing (Beurg et al., 2010; Safieddine et al., 2012). A lower-affinity Ca^{2+} sensor, such as synaptotagmin I, in addition to a loose distribution of Ca^{2+} channels at the ribbons (Wong et al., 2014), may contribute to the nonlinear low Ca^{2+} efficiency of exocytosis in early immature IHCs.

What can hair cells gain from having a high-affinity Ca^{2+} sensor? Considering that otoferlin is involved in both the vesicular fusion and the resupply process (Roux et al., 2006; Pangrsic et al., 2010), a high-affinity Ca^{2+} sensor would not only be instantaneously saturated near the Ca^{2+} channels but also be effectively activated at large distance from the active zone (i.e., at low micromolar Ca^{2+} concentration for an effective vesicle recruitment). The duality of this Ca^{2+} sensing process, possibly placing the vesicle resupply as the rate-limiting step, would allow both VHC-I and IHCs to sustain transmitter release during long stimulations.

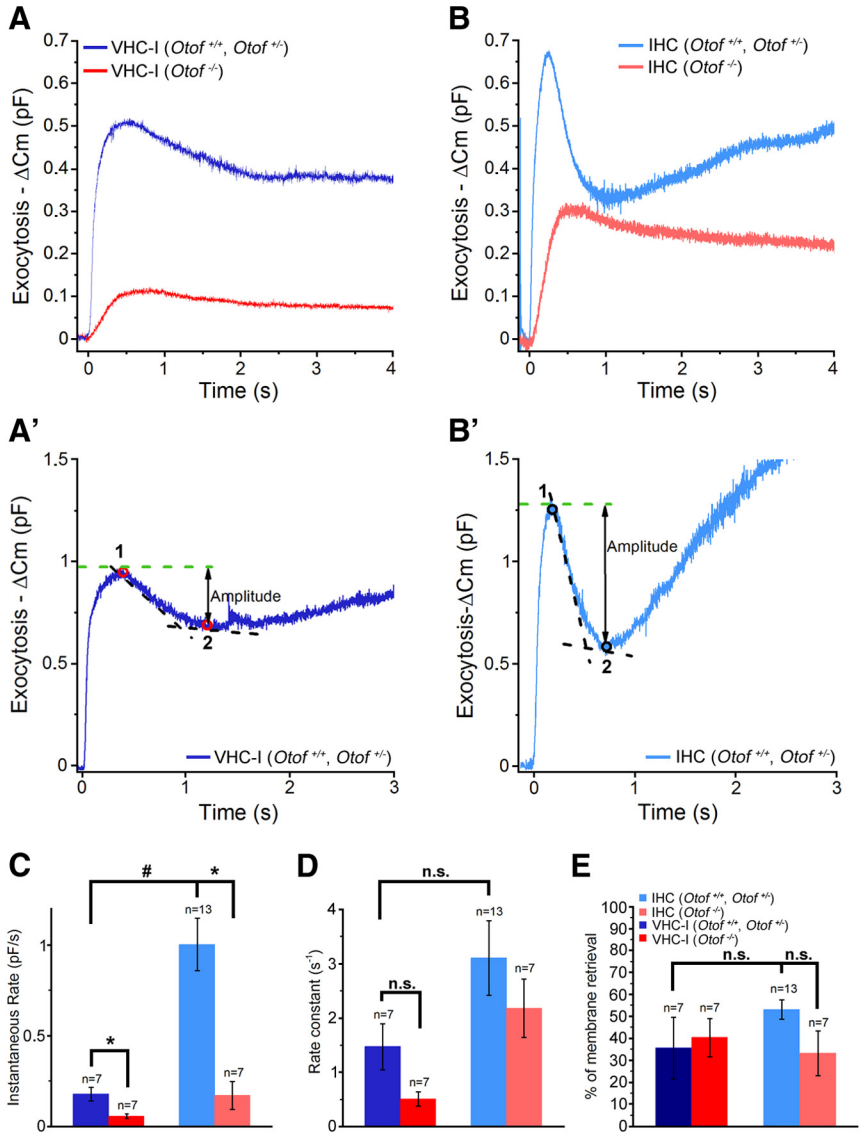

Figure 10. Endocytosis in VHC-I and IHCs. ***A***, A single high-intensity UV flash rising $[Ca^{2+}]_i$ near 80 μM (data not shown) produced a large Δ_{Cm} response in control VHC-I (dark blue line, mean of 7 cells) and a reduced Δ_{Cm} response *in Otof* $^{-/-}$ VHC-I (red line, mean of 7 cells). ***B***, Same as in ***A*** but in control IHCs (light blue line, mean of 13 cells) and in *Otof* $^{-/-}$ IHCs (red line, mean of 7 cells). ***A'***, ***B'***, Example of endocytosis in VHC-I and IHCs, respectively. Endocytosis was essentially analyzed as described by Neef et al. (2014). Briefly, the amplitude of fast endocytosis was measured as the difference between the maximum Δ_{Cm} ("1") and the point where the rate of endocytosis is reduced to 5% of the instantaneous rate ("2"). To calculate the endocytotic instantaneous rate, we used a linear fit function at the point giving the faster rate between point "1" and point "2". ***C***, Histogram plot of the endocytotic instantaneous rate obtained in each group. We found a reduced instantaneous rate in *Otof* $^{-/-}$ VHC-I compared with VHC-I controls ($p = 0.011$) but also in *Otof* $^{-/-}$ IHCs compared with IHCs controls ($p = 0.006$). ***D***, Rate constants were obtained after normalizing the instantaneous rate to the amplitude of endocytosis. No statistical differences were found between control and *Otof* $^{-/-}$ mice (VHC-I, $p = 0.051$; IHCs, $p = 0.55$). ***E***, Percentage of membrane retrieval at the point corresponding to 5% of the maximal instantaneous rate (point "2") normalized by the amplitude of exocytosis (("1" − "2")/"1" × 100). The absence of otoferlin did not interfere with the endocytotic capability of VHC-I and IHCs. ***C–E***, Results are expressed as mean ± SEM. *$p <$ 0.05. #$p <$ 0.001. n.s., No statistical difference.

Ca^{2+}-dependent and otoferlin-independent fast endocytosis

Sustained high rates of vesicle fusion at the hair cell synapses imply a fast mechanism of endocytosis (Beutner et al., 2001; Neef et al., 2014). Here, we found that both VHC-I and IHCs displayed fast endocytotic properties with rather similar time constants. An apparent Ca^{2+} affinity ranging between 7 and 10 μM was estimated in both types of hair cells. Furthermore, we found that the relative endocytotic rate was unaffected in VHC-I and IHCs lacking otoferlin. These results suggested that the fast endocytotic process does not require otoferlin.

Otoferlin is thought to couple clathrin-mediated endocytosis in mature IHCs (Duncker et al., 2013). However, endocytosis associated with the coating activity of clathrin proteins appears too slow to entirely equilibrate the extremely high rate of exocytotic vesicle fusion in hair cells. Therefore, this clathrin-mediated process might represent only a slow component of hair cell endocytosis. Other fast mechanisms, such as bulk endocytosis, probably take place in hair cells (Neef et al., 2014).

Ca^{2+} channel density and spatial organization at the ribbon synapses

Previous studies in *Cav1.3* $^{-/-}$ mice have shown that Cav1.3 channels carry ~90% of total Ca^{2+} currents in IHCs (Platzer et al., 2000; Brandt et al., 2003). In vestibular hair cells, only 50% of total Ca^{2+} currents are driven by Cav1.3 channels (Dou et al., 2004). Additional calcium channels, such as T-type (Nie et al., 2008), N-type (Su et al., 1995), and/or R-type Ca^{2+} channels (Martini et al., 2000), probably take part in the VHC-I Ca^{2+}

influx. Here, we found that Ca^{2+} currents and exocytosis in VHC-I showed a voltage dependence that was shifted by ~10 mV toward negative potentials compared with IHCs. A similar highly negative voltage dependence of Ca^{2+} currents has been described in mouse (Bao et al., 2003), rat (Almanza et al., 2003), and chicken VHC-I (Zampini et al., 2006). Because VHC-I have a highly negative resting potential because of their specific large K^+ conductance $g_{K,L}$ (Rüsch et al., 1998; Brichta et al., 2002), low-voltage activated Ca^{2+} currents would facilitate quantal transmission in these cells. Hair cells from the bullfrog amphibian papilla also display Ca^{2+} current with highly negative voltage dependence and multiquantal release can be triggered at these very negative hair cell membrane potentials (Li et al., 2009; Graydon et al., 2011).

The manner in which auditory and vestibular hair cell afferent ribbon synapses encode different sensory mechanical signals is not well understood. In particular, auditory hair cell synapses discriminate and encode complex acoustic signals over a wide range of frequencies (20 Hz to 20 kHz, in human) and across a wide dynamic range of sound intensity (0–120 dB SPL) by modulating their firing rate from a few 10s of Hertz to 1 kHz (Kiang, 1965; Taberner and Liberman, 2005). Vestibular hair cell synapses primarily code for head velocity over a low-frequency range by modulating their firing rate with short-term dynamics above and below a high resting level of 30–100 spikes/s (Goldberg and Fernandez, 1971; Yang and Hullar, 2007). In addition to conventional cochlear-like afferent bouton terminals on Type II hair cells, the mammalian vestibular epithelia have large afferent calyx terminals that surround VHC-I (Wersäll, 1956; Lysakowski and Goldberg, 2008). Furthermore, VHC-I calyx transmission is thought to involve not only a conventional quantal glutamatergic release but also a nonquantal component likely mediated by ephatic electric coupling and/or by K^+ accumulation in the large calyceal synaptic cleft (Holt et al., 2007; Songer and Eatock, 2013). The role of nonquantal transmission is unknown, but it could boost signaling speed and/or participate in maintaining the resting firing frequency of the calyceal afferent fibers.

Are the mechanisms of glutamatergic vesicular release similar in cochlear and vestibular hair cells? Remarkably, we found that voltage-activated RRP exocytosis displayed higher Ca^{2+} sensitivity in VHC-I than in IHCs. This is likely because of a tighter spatial organization of Ca^{2+} channels at the VHC-I ribbons rather than to a different intrinsic Ca^{2+} affinity of the sensor. A looser coupling of Ca^{2+} channels likely allows a better tuning by endogenous Ca^{2+} buffers as suggested at hippocampal synapses (Vyleta and Jonas, 2014). This organization might produce a more efficient gradual summation of Ca^{2+} at the IHC active zone (Kim et al., 2013), thereby explaining the larger firing dynamic range of auditory fibers compared with vestibular fibers. Coupling of Ca^{2+} influx changes with IHC development (Wong et al., 2014) and also varies between low-threshold and high-threshold ribbon synapses (Frank et al., 2009). A loose coupling organization associated with a relatively low level of endogenous Ca^{2+} buffering proteins in IHCs (Hackney et al., 2005) may also be essential for an efficient recruitment of a distant vesicular resupply machinery. In conclusion, our findings suggest that auditory bouton synapses and vestibular calyceal synapses tune their synaptic firing properties by varying spatial distribution and gating of Ca^{2+} channels at their hair cell pre-synaptic ribbons rather than by using a different Ca^{2+} sensor.

References

Almanza A, Vega R, Soto E (2003) Calcium current in type I hair cells isolated from the semicircular canal crista ampullaris of the rat. Brain Res 994:175–180. CrossRef Medline

Bao H, Wong WH, Goldberg JM, Eatock RA (2003) Voltage-gated calcium channel currents in type I and type II hair cells isolated from the rat crista. J Neurophysiol 90:155–164. CrossRef Medline

Bartoletti TM, Jackman SL, Babai N, Mercer AJ, Kramer RH, Thoreson WB (2011) Release from the cone ribbon synapse under bright light conditions can be controlled by the opening of only a few Ca^{2+} channels. J Neurophysiol 106:2922–2935. CrossRef Medline

Beurg M, Michalski N, Safieddine S, Bouleau Y, Schneggenburger R, Chapman ER, Petit C, Dulon D (2010) Control of exocytosis by synaptotagmins and otoferlin in auditory hair cells. J Neurosci 30:13281–13290. CrossRef Medline

Beutner D, Voets T, Neher E, Moser T (2001) Calcium dependence of exocytosis and endocytosis at the Cochlear inner hair cell afferent synapse. Neuron 29:681–690. CrossRef Medline

Bolte S, Cordelières FP (2006) A guided tour into subcellular co-localization analysis in light microscopy. J Microsc 224:213–232. CrossRef Medline

Brandt A, Striessnig J, Moser T (2003) Ca(V)1.3 channels are essential for development and presynaptic activity of cochlear inner hair cells. J Neurosci 23:10832–10840. Medline

Brandt A, Khimich D, Moser T (2005) Few Ca(V)1.3 channels regulate the exocytosis of a synaptic vesicle at the hair cell ribbon synapse. J Neurosci 25:11577–11585. CrossRef Medline

Brichta AM, Aubert A, Eatock RA, Goldberg JM (2002) Regional analysis of whole cell currents from hair cells of the turtle posterior crista. J Neurophysiol 88:3259–3278. CrossRef Medline

Brose N, Petrenko AG, Südhof TC, Jahn R (1992) Synaptotagmin: a calcium sensor on the synaptic vesicle surface. Science 256:1021–1025. CrossRef Medline

Brown AM, Kunze DL, Yatani A (1984) The agonist effect of dihydropyridines on Ca-channels. Nature 311:570–572. CrossRef Medline

Bucurenciu I, Kulik A, Schwaller B, Frotscher M, Jonas P (2008) Nanodomain coupling between Ca^{2+} channels and Ca^{2+} sensors promotes fast and efficient transmitter release at a cortical GABAergic synapse. Neuron 57:536–545. CrossRef Medline

Cho S, Li GL, von Gersdorff H (2011) Recovery from short-term depression and facilitation is ultrafast and Ca^{2+} dependent at auditory hair cell synapses. J Neurosci 31:5682–5692. CrossRef Medline

Davis AF, Bai J, Fasshauer D, Wolowick MJ, Lewis JL, Chapman ER (1999) Kinetics of synaptotagmin responses to Ca^{2+} and assembly with the core SNARE complex onto membranes. Neuron 24:363–376. CrossRef Medline

Di Biase V, Obermair GJ, Szabo Z, Altier C, Sanguesa J, Bourinet E, Flucher BE (2008) Stable membrane expression of postsynaptic Ca(V)1.2 calcium channel clusters is independent of interactions with AKAP79/150 and PDZ proteins. J Neurosci 28:13845–13855. CrossRef Medline

Dou H, Vazquez AE, Namkung Y, Chu H, Cardell EL, Nie L, Parson S, Shin HS, Yamoah EN (2004) Null mutation of alpha(1D) Ca^{2+} channel gene results in deafness but no vestibular defect in mice. J Assoc Res Otolaryngol 5:215–226. CrossRef Medline

Dulon D, Safieddine S, Jones SM, Petit C (2009) Otoferlin is critical for a highly sensitive and linear calcium-dependent exocytosis at vestibular hair cell ribbon synapses. J Neurosci 29:10474–10487. CrossRef Medline

Duncker SV, Franz C, Kuhn S, Schulte U, Campanelli D, Brandt N, Hirt B, Fakler B, Blin N, Ruth P, Engel J, Marcotti W, Zimmermann U, Knipper M (2013) Otoferlin couples to clathrin-mediated endocytosis in mature cochlear inner hair cells. J Neurosci 33:9508–9519. CrossRef Medline

Eatock RA, Songer JE (2011) Vestibular hair cells and afferents: two channels for head motion signals. Annu Rev Neurosci 34:501–534. CrossRef Medline

Eggermann E, Bucurenciu I, Goswami SP, Jonas P (2011) Nanodomain coupling between Ca^{2+} channels and sensors of exocytosis at fast mammalian synapses. Nat Rev Neurosci 13:7–21. CrossRef Medline

Ehret G (1983) Development of hearing and response behavior to sound stimuli: behavioral studies. In: Development of auditory and vestibular systems (Romand R, ed), pp 211–234. San Diego: Academic.

Ellis-Davies GC, Kaplan JH, Barsotti RJ (1996) Laser photolysis of caged calcium: rates of calcium release by nitrophenyl-EGTA and DM-nitrophen. Biophys J 70:1006–1016. CrossRef Medline

Favre D, Sans A (1979) Morphological changes in afferent vestibular hair cell synapses during the postnatal development of the cat. J Neurocytol 8:765–775. CrossRef Medline

Frank T, Khimich D, Neef A, Moser T (2009) Mechanisms contributing to synaptic Ca^{2+} signals and their heterogeneity in hair cells. Proc Natl Acad Sci U S A 106:4483–4488. CrossRef Medline

Fuchs PA (2005) Time and intensity coding at the hair cell's ribbon synapse. J Physiol 566:7–12. CrossRef Medline

Glowatzki E, Fuchs PA (2002) Transmitter release at the hair cell ribbon synapse. Nat Neurosci 5:147–154. CrossRef Medline

Goldberg JM, Fernandez C (1971) Physiology of peripheral neurons innervating semicircular canals of the squirrel monkey: I. Resting discharge and response to constant angular accelerations. J Neurophysiol 34:635–660. Medline

Goutman JD, Glowatzki E (2007) Time course and calcium dependence of transmitter release at a single ribbon synapse. Proc Natl Acad Sci U S A 104:16341–16346. CrossRef Medline

Grant L, Yi E, Glowatzki E (2010) Two modes of release shape the postsynaptic response at the inner hair cell ribbon synapse. J Neurosci 30:4210–4220. CrossRef Medline

Graydon CW, Cho S, Li GL, Kachar B, von Gersdorff H (2011) Sharp Ca^{2+} nanodomains beneath the ribbon promote highly synchronous multivesicular release at hair cell synapses. J Neurosci 31:16637–16650. CrossRef Medline

Hackney CM, Mahendrasingam S, Penn A, Fettiplace R (2005) The concentrations of calcium buffering proteins in mammalian cochlear hair cells. J Neurosci 25:7867–7875. CrossRef Medline

Hall JD, Betarbet S, Jaramillo F (1997) Endogenous buffers limit the spread of free calcium in hair cells. Biophys J 73:1243–1252. CrossRef Medline

Heil P, Neubauer H (2010) Summing across different active zones can explain the quasi-linear Ca^{2+}-dependencies of exocytosis by receptor cells. Front Synaptic Neurosci 2:148. CrossRef Medline

Holt JC, Chatlani S, Lysakowski A, Goldberg JM (2007) Quantal and nonquantal transmission in calyx-bearing fibers of the turtle posterior crista. J Neurophysiol 98:1083–1101. CrossRef Medline

Huterer M, Cullen KE (2002) Vestibuloocular reflex dynamics during high-frequency and high-acceleration rotations of the head on body in rhesus monkey. J Neurophysiol 88:13–28. Medline

Johnson CP, Chapman ER (2010) Otoferlin is a calcium sensor that directly regulates SNARE-mediated membrane fusion. J Cell Biol 191:187–197. CrossRef Medline

Johnson SL, Marcotti W, Kros CJ (2005) Increase in efficiency and reduction in Ca^{2+} dependence of exocytosis during development of mouse inner hair cells. J Physiol 563:177–191. CrossRef Medline

Johnson SL, Forge A, Knipper M, Münkner S, Marcotti W (2008) Tonotopic variation in the calcium dependence of neurotransmitter release and vesicle pool replenishment at mammalian auditory ribbon synapses. J Neurosci 28:7670–7678. CrossRef Medline

Johnson SL, Beurg M, Marcotti W, Fettiplace R (2011) Prestin-driven cochlear amplification is not limited by the outer hair cell membrane time constant. Neuron 70:1143–1154. CrossRef Medline

Jones TA, Jones SM (2007) Vestibular evoked potentials. In: Auditory evoked potentials: basic principles and clinical application (Burkard RF, Eggermont JJ, Don M, eds). Philadelphia: Lippincott Williams and Wilkins.

Kantardzhieva A, Liberman MC, Sewell WF (2013) Quantitative analysis of ribbons, vesicles, and cisterns at the cat inner hair cell synapse: correlations with spontaneous rate. J Comp Neurol 521:3260–3271. CrossRef Medline

Kiang NY (1965) Discharge patterns of single fibers in the cat's auditory nerve. Cambridge, MA: Massachusetts Institute of Technology.

Kim MH, Li GL, von Gersdorff H (2013) Single Ca^{2+} channels and exocytosis at sensory synapses. J Physiol 591:3167–3178. Medline

Lai SK, Lai CH, Tse YC, Yung KK, Shum DK, Chan YS (2008) Developmental maturation of ionotropic glutamate receptor subunits in rat vestibular nuclear neurons responsive to vertical linear acceleration. Eur J Neurosci 28:2157–2172. CrossRef Medline

Lenzi D, Runyeon JW, Crum J, Ellisman MH, Roberts WM (1999) Synaptic vesicle populations in saccular hair cells reconstructed by electron tomography. J Neurosci 19:119–132. Medline

Levic S, Bouleau Y, Dulon D (2011) Developmental acquisition of a rapid calcium-regulated vesicle supply allows sustained high rates of exocytosis in auditory hair Cells. PLoS One 6:e25714. CrossRef Medline

Li GL, Keen E, Andor-Ardó D, Hudspeth AJ, von Gersdorff H (2009) The unitary event underlying multiquantal EPSCs at a hair cell's ribbon synapse. J Neurosci 29:7558–7568. CrossRef Medline

Liberman LD, Wang H, Liberman MC (2011) Opposing gradients of ribbon size and AMPA receptor expression underlie sensitivity differences among cochlear-nerve/hair-cell synapses. J Neurosci 31:801–808. CrossRef Medline

Liberman MC, Dodds LW, Pierce S (1990) Afferent and efferent innervation of the cat cochlea: quantitative analysis with light and electron microscopy. J Comp Neurol 301:443–460. CrossRef Medline

Lysakowski A, Goldberg JM (2008) Ultrastructural analysis of the cristae ampullares in the squirrel monkey (Saimiri sciureus). J Comp Neurol 511:47–64. CrossRef Medline

Lysakowski A, Gaboyard-Niay S, Calin-Jageman I, Chatlani S, Price SD, Eatock RA (2011) Molecular microdomains in a sensory terminal, the vestibular calyx ending. J Neurosci 31:10101–10114. CrossRef Medline

Martini M, Rossi ML, Rubbini G, Rispoli G (2000) Calcium currents in hair cells isolated from semicircular canals of the frog. Biophys J 78:1240–1254. CrossRef Medline

Meyer AC, Frank T, Khimich D, Hoch G, Riedel D, Chapochnikov NM, Yarin YM, Harke B, Hell SW, Egner A, Moser T (2009) Tuning of synapse number, structure and function in the cochlea. Nat Neurosci 12:444–453. CrossRef Medline

Naraghi M, Neher E (1997) Linearized buffered Ca^{2+} diffusion in microdomains and its implications for calculation of Ca^{2+} at the month of a calcium channel. J Neurosci 17:6961–6973. Medline

Neef J, Jung S, Wong AB, Reuter K, Pangrsic T, Chakrabarti R, Kügler S, Lenz C, Nouvian R, Boumil RM, Frankel WN, Wichmann C, Moser T (2014) Modes and regulation of endocytic membrane retrieval in mouse auditory hair cells. J Neurosci 34:705–716. CrossRef Medline

Neher E (1998) Usefulness and limitations of linear approximations to the understanding of Ca^{2+} signals. Cell Calcium 24:345–357. CrossRef Medline

Nie L, Zhu J, Gratton MA, Liao A, Mu KJ, Nonner W, Richardson GP, Yamoah EN (2008) Molecular identity and functional properties of a novel T-type Ca^{2+} channel cloned from the sensory epithelia of the mouse inner ear. J Neurophysiol 100:2287–2299. CrossRef Medline

Palmer AR, Russell IJ (1986) Phase-locking in the cochlear nerve of the guinea-pig and its relation to the receptor potential of inner hair cells. Hear Res 24:1–15. CrossRef Medline

Pangrsic T, Lasarow L, Reuter K, Takago H, Schwander M, Riedel D, Frank T, Tarantino LM, Bailey JS, Strenzke N, Brose N, Müller U, Reisinger E, Moser T (2010) Hearing requires otoferlin-dependent efficient replenishment of synaptic vesicles in hair cells. Nat Neurosci 13:869–876. CrossRef Medline

Platzer J, Engel J, Schrott-Fischer A, Stephan K, Bova S, Chen H, Zheng H, Striessnig J (2000) Congenital deafness and sinoatrial node dysfunction in mice lacking class D L-type Ca^{2+} channels. Cell 102:89–97. CrossRef Medline

Rennie KJ, Streeter MA (2006) Voltage-dependent currents in isolated vestibular afferent calyx terminals. J Neurophysiol 95:26–32. CrossRef Medline

Roberts WM, Jacobs RA, Hudspeth AJ (1990) Co-localization of ion channels involved in frequency-selectivity and synaptic transmission at presynaptic active zones of hair cells. J Neurosci 10:3664–3684. Medline

Roux I, Safieddine S, Nouvian R, Grati M, Simmler MC, Bahloul A, Perfettini I, Le Gall M, Rostaing P, Hamard G, Triller A, Avan P, Moser T, Petit C (2006) Otoferlin, defective in a human deafness form, is essential for exocytosis at the auditory ribbon synapse. Cell 127:277–289. CrossRef Medline

Rüsch A, Lysakowski A, Eatock RA (1998) Postnatal development of type I and type II hair cells in the mouse utricle: acquisition of voltage-gated conductances and differentiated morphology. J Neurosci 18:7487–7501. Medline

Safieddine S, El-Amraoui A, Petit C (2012) The auditory hair cell ribbon synapse: from assembly to function. Annu Rev Neurosci 35:509–528. CrossRef Medline

Schnee ME, Ricci AJ (2003) Biophysical and pharmacological characterization of voltage-gated calcium currents in turtle auditory hair cells. J Physiol 549:697–717. CrossRef Medline

Schnee ME, Lawton DM, Furness DN, Benke TA, Ricci AJ (2005) Auditory hair cell-afferent fiber synapses are specialized to operate at their best frequencies. Neuron 47:243–254. CrossRef Medline

Schnee ME, Santos-Sacchi J, Castellano-Muñoz M, Kong JH, Ricci AJ (2011) Calcium-dependent synaptic vesicle trafficking underlies indefatigable release at the hair cell afferent fiber synapse. Neuron 70:326–338. CrossRef Medline

Smith CA, Sjostrand FS (1961) Structure of the nerve endings on the external hair cells of the guinea pig cochlea as studied by serial sections. J Ultrastruct Res 5:523–556. CrossRef Medline

Sobkowicz HM, Rose JE, Scott GE, Slapnick SM (1982) Ribbon synapses in the developing intact and cultured organ of Corti in the mouse. J Neurosci 2:942–957. Medline

Songer JE, Eatock RA (2013) Tuning and timing in mammalian type I hair cells and calyceal synapses. J Neurosci 33:3706–3724. CrossRef Medline

Su ZL, Jiang SC, Gu R, Yang WP (1995) Two types of calcium channels in bullfrog saccular hair cells. Hear Res 87:62–68. CrossRef Medline

Taberner AM, Liberman MC (2005) Response properties of single auditory nerve fibers in the mouse. J Neurophysiol 93:557–569. CrossRef Medline

Van Hook MJ, Thoreson WB (2012) Rapid synaptic vesicle endocytosis in cone photoreceptors of salamander retina. J Neurosci 32:18112–18123. CrossRef Medline

Vyleta NP, Jonas P (2014) Loose coupling between Ca^{2+} channels and release sensors at a plastic hippocampal synapse. Science 343:665–670. CrossRef Medline

Wersäll J (1956) Studies on the structure and innervation of the sensory epithelium of the cristae ampulares in the guinea pig: a light and electron microscopic investigation. Acta Otolaryngol Suppl 126:1–85. Medline

Wersäll J, Gleisner L, Lundquist PG (1967) Vestibular mechanism: fine structure. Ultrastructure of the vestibular end organs. Ciba Found Symp 105–120.

Wong AB, Rutherford MA, Gabrielaitis M, Pangrsic T, Göttfert F, Frank T, Michanski S, Hell S, Wolf F, Wichmann C, Moser T (2014) Developmental refinement of hair cell synapses tightens the coupling of Ca^{2+} influx to exocytosis. EMBO J 33:247–264. CrossRef Medline

Wu XS, Wu LG (2014) The yin and yang of calcium effects on synaptic vesicle endocytosis. J Neurosci 34:2652–2659. CrossRef Medline

Wu YC, Tucker T, Fettiplace R (1996) A theoretical study of calcium microdomains in turtle hair cells. Biophys J 71:2256–2275. CrossRef Medline

Yang A, Hullar TE (2007) Relationship of semicircular canal size to vestibular-nerve afferent sensitivity in mammals. J Neurophysiol 98:3197–3205. CrossRef Medline

Zampini V, Valli P, Zucca G, Masetto S (2006) Single-channel L-type Ca^{2+}-currents in chicken embryo semicircular canal type I and type II hair cells. J Neurophysiol 96:602–612. CrossRef Medline

Zampini V, Johnson SL, Franz C, Lawrence ND, Münkner S, Engel J, Knipper M, Magistretti J, Masetto S, Marcotti W (2010) Elementary properties of Ca(V)1.3 Ca^{2+} channels expressed in mouse cochlear inner hair cells. J Physiol 588:187–199. CrossRef Medline

Zidanic M, Fuchs PA (1995) Kinetic analysis of barium currents in chick cochlear hair cells. Biophys J 68:1323–1336. CrossRef Medline